

**Flare Energy Release at the Magnetic Field Polarity Inversion  
Line During M1.2 Solar Flare of 2015 March 15. II. Investigation  
of Photospheric Electric Current and Magnetic Field Variations  
Using HMI 135-second Vector Magnetograms**

I.N. Sharykin<sup>1</sup>, I.V. Zimovets<sup>1</sup>, I.I. Myshyakov<sup>2</sup>

Space Research Institute of Russian Academy of Sciences (IKI), Moscow, Russia

Received \_\_\_\_\_; accepted \_\_\_\_\_

---

<sup>1</sup>Space Research Institute (IKI) of the Russian Academy of Sciences

<sup>2</sup>Institute of Solar-Terrestrial Physics (ISTP) of the Russian Academy of Sciences,  
Siberian Branch

## ABSTRACT

This work is a continuation of Paper I (Sharykin et al. 2018) devoted to analysis of nonthermal electron dynamics and plasma heating in the confined M1.2 class solar flare SOL2015-03-15T22:43 revealing energy release in the highly sheared interacting magnetic loops in the low corona, above the polarity inversion line (PIL). The scope of the present work is to make the first extensive quantitative analysis of the photospheric magnetic field and photospheric vertical electric current (PVEC) dynamics in the PIL region using new vector magnetograms obtained with the Helioseismic and Magnetic Imager (HMI) onboard the Solar Dynamics Observatory (SDO) with high temporal resolution of 135 s. Data analysis revealed sharp changes of the magnetic structure and PVEC associated with the flare onset near the PIL. It was found that the strongest plasma heating and electron acceleration were associated with the largest increase of the magnetic reconnection rate, total PVEC and effective PVEC density in the flare ribbons. Observations and non-linear force-free field (NLFFF) extrapolations have shown that the magnetic field structure around the PIL is consistent with the tether-cutting magnetic reconnection (TCMR) geometry. We gave qualitative interpretation of the observed dynamics of the flare ribbons, magnetic field and PVEC, and electron acceleration, within the TCMR scenario.

*Subject headings:* Sun: chromosphere; Sun: corona; Sun: flares; Sun: magnetic fields; Sun: photosphere

## 1. INTRODUCTION

Initiation of solar flares is connected with magnetic field dynamics in active regions of the Sun. Free magnetic energy contained in active regions in the form of electrical currents is enough to explain any small and large, confined and eruptive solar flares (Emslie et al. 2012; Aschwanden et al. 2014). One of the key observational objects determining magnetic field topology of active regions is the photospheric polarity inversion line (PIL). It has been known since the observations of Severnyi (1958) that solar flares appear near the PIL of the line-of-sight (LOS) magnetic field (e.g. Rust 1972; Schrijver 2009; Sadykov & Kosovichev 2017). The recent statistical study by Schrijver (2016) illustrated that X-class flares are associated with strong-field, high-gradient polarity inversion lines (SHIL) created during the emergence of magnetic flux. Many recent works (e.g. Chifor et al. 2007; Zimovets et al. 2009; Bamba et al. 2017; Wang et al. 2017) also reported pre-flare activity around the PIL in the form of brightenings seen in different ranges of the electromagnetic spectrum. Thus, observations of the PIL regions are crucial for understanding the processes of accumulation and release of energy in solar flares.

Strong changes of magnetic field on the photosphere near the PIL during flares were reported in many works (e.g. Wang et al. 1994; Kosovichev & Zharkova 2001; Sudol & Harvey 2005; Petrie 2013; Fainshtein et al. 2016; Wang et al. 2018). In particular, according to (Sun et al. 2012; Petrie 2013) magnetic field near the PIL became stronger and more horizontal, and the magnetic shear increased during flares. It was also found that the horizontal gradient of radial magnetic field can increase during a flare (e.g. Sharykin et al. 2017). The nonlinear force-free field (NLFFF) extrapolations have shown that magnetic field lines around the PIL became shorter during flares (e.g. Sun et al. 2012; Sharykin & Kosovichev 2015). Probably, such behavior of magnetic loops can be connected with the process of magnetic reconnection above the photospheric PIL during flares.

According to the main modern paradigm, the primary energy release of solar flares, accompanied by the transformation of free magnetic energy into the kinetic energy of heated plasma and accelerated particles and radiation, occurs in the corona as a result of magnetic reconnection above the photospheric PIL (Priest & Forbes 2002; Aschwanden 2004; Shibata & Magara 2011). In a common situation, where there is one main PIL in an active region, a flare occurs in a bipolar magnetic configuration. Usually this bipolar structure is an arcade of sheared magnetic loops or a twisted magnetic flux rope embedded in the arcade along the PIL. Conventionally, the innermost part of the magnetic arcade is called the core field, and the outer layers are called the envelope fields (Moore & Roumeliotis 1992; Moore et al. 2001). The core field lines are highly sheared, such they can almost be parallel to the PIL. The core field lines can constitute a magnetic flux-rope before a flare, or form it as a result of the magnetic reconnection during a flare (e.g Gibson et al. 2004, 2006; Wang et al. 2015; Cheng et al. 2017). The reconnection can also result in the increase of magnetic flux and twist of a pre-existing flux-rope.

The flare and eruption can be triggered in various ways in the bipolar magnetic configuration (e.g. Priest 2014). In particular, the widely discussed possibilities include (but not limited by) various instabilities of a magnetic flux-rope (e.g. Hood & Priest 1979; Gibson et al. 2004; Török & Kliem 2005; Kliem & Török 2006), or the so-called tether-cutting magnetic reconnection (TCMR) of the core field leading to formation of an unstable flux-rope (Moore & Roumeliotis 1992; Moore et al. 2001). The TCMR concept considers the situation when a group of highly sheared field lines interact and reconnect above the PIL, forming two new groups of field lines: one group of lower-lying, shorter and less sheared loops than initial field lines, and another group of higher field lines forming (or contributing to) a magnetic flux-rope. In such a scenario, a flare may develop in two consecutive or partially overlapping phases. The first phase is related to the TCMR or the so-called “zipper-reconnection” (Priest & Longcope 2017; Threlfall et al. 2018), and

is associated with the apparent systematic motion of  $H_\alpha$ , ultraviolet (UV), soft and hard X-ray (SXR and HXR, respectively) emission sources along the PIL, and the elongation of flare ribbons (e.g. Vorpahl 1976; Krucker et al. 2003; Bogachev et al. 2005; Grigis & Benz 2005; Qiu 2009; Yang et al. 2009; Zimovets & Struminsky 2009; Kuznetsov et al. 2016; Qiu et al. 2017). This first phase usually coincides with the flare impulsive phase, often accompanied by successive bursts or pulsations of energetic electromagnetic radiation. The second phase is related to formation of a three-dimensional quasi-vertical current sheet beneath an erupting flux-rope and magnetic reconnection in this current sheet. This phase is predominantly accompanied by expansion and separation of flare ribbons away from the PIL, and is well-explained by the “standard” (CSHKP) two-dimensional flare model and its three-dimensional extensions (Carmichael 1964; Sturrock 1966; Hirayama 1974; Kopp & Pneuman 1976; Shibata & Magara 2011; Janvier 2017).

One may suggest that depending on the initial configuration of the magnetic field and the development of the process of formation and eruption of a flux-rope, the two phases under consideration can be expressed differently. For example, in the case of the presence of a highly twisted unstable flux-rope before the onset of eruption and its quasi-homogeneous (symmetric) eruption along the PIL, the “zipper-reconnection” phase may be very quick or absent, and the motion along the PIL is not pronounced. In the event when a flux-rope eruption cannot fully develop, i.g., due to a strongly suppressing overlying magnetic field, the second phase of flare ribbon expansion may be mild or absent, and one observes a confined flare (e.g. Thalmann et al. 2015; Amari et al. 2018). It should be noted here that the observed speeds of movement of the flare footpoint sources are used to estimate such an important physical quantity as the reconnection electric field ( $E$ ) and dimensionless reconnection rate in the coronal energy release sources, i.e. the Alfvén Mach number  $M_A = v_{in}/v_A$ , where  $v_{in}$  and  $v_A$  are the inflow and Alfvén speeds respectively (e.g. Forbes & Lin 2000; Qiu et al. 2002; Isobe et al. 2002; Asai et al. 2004; Isobe et al. 2005; Miklenic

et al. 2007; Yang et al. 2011; Hinterreiter et al. 2018). The values found in this way are in the ranges of  $E \sim 1 - 100 \text{ V cm}^{-1}$  and  $M_A \sim 0.001 - 0.1$ .

Since the free energy in the active regions is contained in the form of electric currents flowing along magnetic field lines or having the form of current sheets, currents play an important role in the processes of flare energy release (Melrose 2017; Fleishman & Pevtsov 2018; Schmieder & Aulanier 2018). However, routine measurements of electric currents in the corona are not available yet. Measurements of the photospheric magnetic field vector in the active regions producing solar flares reveal sites of enhanced vertical electric currents in the vicinity of the PIL (e.g. Moreton & Severny 1968; Leka et al. 1993; van Driel-Gesztelyi et al. 1994; Janvier et al. 2014; Sharykin & Kosovichev 2015; Janvier et al. 2016; Wang et al. 2018). Using vector magnetograms with high spatial resolution (up to 100 km) from the New Solar Telescope (NST) of the Big Bear Solar Observatory (BBSO) Wang et al. (2017) have shown that pre-flare activity in the form of optical brightenings near the PIL is associated with multiple inversions of the radial magnetic field and regions of enhanced photospheric vertical electric currents (PVEC).

One can suspect that electrons accelerated in the sheared magnetic structures, possibly associated with magnetic flux-ropes and/or the TCMR, may correspond to the regions of enhanced PVEC, as they trace twisted magnetic field lines stretched along the PIL. Many observations (e.g. Romanov & Tsap 1990; Abramenko et al. 1991; Canfield et al. 1992; Leka et al. 1993; Démoulin et al. 1996) have shown that flare  $H_\alpha$  or HXR emission sources do not exactly correspond to the most intensive PVEC. In particular, it was demonstrated by Li et al. (1997) that the sites of accelerated electrons precipitation to the chromosphere, found from the observations of the Hard X-ray Telescope (HXT) onboard Yohkoh, avoid the sites of the highest PVEC density and occur adjacent to these current channels. The recent studies by Musset et al. (2015); Sharykin et al. (2015) using vector magnetograms

from the Helioseismic and Magnetic Imager (HMI; Scherrer et al. (2012)) onboard the Solar Dynamics Observatory (SDO; Pesnell et al. (2012)) have shown that only a part of the HXR emission sources are located in the vicinity of the enhanced PVEC near the PIL. This indicates the absence of a direct spatial connection between the enhanced vertical electric currents and beams of accelerated particles. Musset et al. (2015) have also demonstrated co-spatial appearance of a new HXR source and a region of new enhanced PVEC during the same period of the powerful eruptive X2.2 flare on 15 February 2011. Moreover, it was shown recently that the photospheric vertical electric currents integrated over the flare regions near the PIL has tendency to increase abruptly and stepwise during some flares (Janvier et al. 2014; Sharykin & Kosovichev 2015; Janvier et al. 2016; Wang et al. 2018). These observations are not consistent with the electric circuit type models (Alfvén & Carlqvist 1967; Colgate 1978; Zaitsev & Stepanov 2015; Zaitsev et al. 2016). Rather they support the concept that the processes of flare energy release and acceleration of particles occur in the coronal reconnection regions above the photospheric PIL. In this case, the presence of regions of enhanced PVEC indicates the presence of free magnetic energy above the PIL, a part of which can be released during a flare. The detected increase of vertical currents and the appearance of new sites of enhanced currents on the photosphere during flares can be interpreted as the generation of new currents in the coronal sources and their closure (at least partial) to or through the photosphere.

The major fraction of recent (since 2010) works dedicated to studying magnetic field and PVEC during flares were made using HMI/SDO vector magnetograms (Centeno et al. 2014; Hoeksema et al. 2014). Angular resolution of standard HMI vector magnetograms is about  $1''$  when temporal resolution is 720 s. Comparing with typical duration of the flare impulsive phase ( $\approx 1 - 10$  min), such time cadence is insufficient to resolve changes of magnetic field during flares. In this situation, one is mainly able to compare pre-flare and post-flare states of magnetic field. However, it is known that electron acceleration and

plasma heating develops on shorter than 12 min time-scales (e.g. Aschwanden 2004). Thus, to understand development of the flare energy release processes one need to investigate dynamics of the flare emission sources, photospheric magnetic field and PVEC with a time resolution significantly less than 12 min.

New high-cadence vector magnetograms from HMI, which recently became in open access, have a large potential for this kind of research. Standard (12-minute) HMI vector magnetograms are the result of summation of 135-second vector magnetograms. The time step of 135 s is an instrumental time needed for measuring the full set of Stokes profiles for calculation of all magnetic field components. Summation of 135-second magnetograms is made for increasing the signal-to-noise ratio. Sun et al. (2017) demonstrated that 135-second magnetograms are more noisy than the standard ones. However, for the magnetic field values larger than 300 G the uncertainty for all magnetic field components is small. Sun et al. (2017) described the high-cadence observations of magnetic field changes during the powerful X2.2 flare of 2011 February 15, which were mostly pronounced for the horizontal magnetic component. Kleint et al. (2018) presented the non-linear force-free field (NLFFF) modeling of the X1 flare region of 2014 March 29 based on 135-second magnetograms. They found that the magnetic field changes on the photosphere and in the chromosphere are surprisingly different, and are unlikely to be reproduced by a force-free model. These works demonstrated that the new HMI data product can be successfully used to study the flare processes in the active regions with strong magnetic fields. However, this data product has not been widely used yet.

The present work is a continuation of our previous work (hereinafter, Paper I, Sharykin et al. 2018). Paper I was devoted to detailed quantitative multiwavelength analysis of nonthermal electron dynamics and plasma heating in the system of highly sheared magnetic loops interacting with each other above the PIL during the first sub-flare of the confined



(non-fully-eruptive) M1.2 class solar flare on 2015 March 15 (SOL2015-03-15T22:43). This flare was selected because there were emission sources in different ranges of electromagnetic spectrum located in the PIL region with strong photospheric horizontal magnetic field and PVEC. The following analysis was performed in Paper I: a) joint spectral analysis of the X-ray and microwave data; b) comparison of the X-ray images with the ultraviolet and optical images; c) analysis of the NLFFF extrapolation results; d) modeling of the microwave gyrosynchrotron emission of nonthermal electrons injected into the low-lying twisted magnetic structure along the PIL using the GX Simulator (Nita et al. 2015). It was found that the observed structure and dynamics of the flare emission sources and magnetic field is consistent with a scenario of the TCMR within the non-neutralized current sheet with the strong guide magnetic field component along the PIL. It was found that nonthermal electrons with the hardest spectrum appeared at the onset of plasma heating up to the super-hot temperature of 40 MK. By simulating the gyrosynchrotron radiation and comparing with observations, it was inferred that the accelerated electrons were localized in a thin magnetic channel with a width of around 0.5 Mm elongated along the PIL within the twisted low-lying ( $\approx 3$  Mm above the photosphere) magnetic structure with the high average magnetic field of about 1200 Gauss. The plasma beta (i.e. the ratio of the plasma pressure to the magnetic pressure) in the super-hot region was  $\beta < 0.01$ . The accelerated electron density in this region above the PIL was about  $10^9 \text{ cm}^{-3}$  that is much less than the density of the thermal super-hot plasma. These physical parameters will be used in the present work.

Despite the detailed analysis of the multiwavelength observations of the flare emission sources and its modeling done in Paper I, there was no investigation of dynamics of photospheric magnetic field and PVEC near the PIL. There was also no discussion of electron acceleration and plasma heating as a consequence of magnetic field and PVEC changes around the PIL. It was just mentioned that the observed flare emission sources

were located close to the PIL, and the HXR sources were almost co-spatial with the regions of strong PVEC found from the standard (12-minute) HMI vector magnetograms.

The goal of the present work is to make extensive quantitative analysis of magnetic field and PVEC dynamics in the SOL2015-03-15T22:43 event near the PIL using new high-cadence, 135-second, HMI/SDO vector magnetograms. It allows to study magnetic reconnection near the PIL accompanied by efficient plasma heating and electron acceleration. The work is aimed at solving the following tasks. The first task is to compare positions of the X-ray sources and flare ribbons with distributions of PVEC, magnetic field components, and the horizontal gradient of the vertical magnetic field on the photosphere. The second task is to determine variations of photospheric magnetic flux and PVEC in the entire PIL region. The third task is to determine variations of the photospheric magnetic field components and PVEC in the developing flare ribbons and to compare these variations with variations of the flare electromagnetic emissions. The fourth task is to estimate electric field in the reconnecting current sheet (and some of its physical parameters) to evaluate potential efficiency of electron acceleration by this field. The reconnection rate will be also estimated. Finally, we will discuss results of the data analysis performed in the frame of the TCMR scenario.

The paper is organized as follows. Section 2 describes some general observations of the flare including vector magnetograms, X-ray and optical images. Analysis of HMI 135-second vector magnetograms and nonlinear force-free field (NLFFF) extrapolations based on these magnetograms are described in Sections 3 and 4, respectively. In Section 5 we present time profiles of different parameters inside the flare ribbons calculated from HMI vector magnetograms. Discussion and conclusions of the results obtained are presented in the two final sections.

## 2. OBSERVATIONS

### 2.1. TIME PROFILES OF FLARE EMISSION

Figure 1 shows temporal evolution of electromagnetic emission light curves of the flare studied. The top panel demonstrates comparison of the radio fluxes detected by the Nobeyama Radio Polarimeter (NoRP) with the SXR flux in 1-8 Å band detected by the X-ray Sensor onboard the Geostationary Operational Environmental Satellite (GOES). The NoRP time profiles are shown for five frequencies: 2, 3.75, 9.4, 17, and 35 GHz. The bottom panel shows the time profiles of the Ramaty High-Energy Solar Spectroscopic Imager (RHESSI; (Lin et al. 2002)) count rate in the energy band of 25-50 keV (grey histogram) and of the time derivatives of the GOES SXR lightcurves. One can see that the flare consists of at least three successive sub-flares. Approximate duration of the corresponding microwave bursts was about 2–5 minutes. We use the logarithmic time scale to demonstrate three subsequent fast impulsive phases of these sub-flares on time scale ( $\sim 100$  minutes) of the whole flare process. This representation also helps to see zoomed time interval of the first subflare, which is the most interesting because of the nonthermal electrons with the hardest spectrum. We also should mention that the observed three bursts are considered as parts of the large flare process, as it is shown (see next sections) that all emission sources and changes of the magnetic field was in the same region near the PIL. Moreover, UV maps revealed continual transition of the energy release from the decay phase of the previous subflare to the impulsive phase of the next subflare. In other words subsequent subflares are developed from the initial magnetic configurations prepared by the previous flare energy release.

The HXR and microwave emissions were generated by accelerated electrons. Intensities of these nonthermal emissions were maximal during the first subflare, which was investigated in details in Paper I. Spectral analysis of the X-ray emission done in the previous work

revealed that the spectrum consists of two components: thermal (SXR,  $\lesssim 20$  keV) and nonthermal (HXR,  $\gtrsim 20$  keV). In particular, detailed modelling of microwave gyrosynchrotron emission was performed, and we remind that the dominating emission at 35 GHz during the first sub-flare is a result of the gyrosynchrotron radiation of nonthermal electrons localized in the low-lying magnetic loops with the average value of the magnetic field  $\approx 1200$  G. Figure 1 also reveals that the HXR and microwave emission peaks correspond to peaks in time derivative of the GOES lightcurves (known as the Neupert effect; Neupert 1968). Further, in this paper, we will use the time derivative of the GOES lightcurve in 1-8 Å band to compare coronal the flare energy release process with the dynamics of the photospheric magnetic fields and PVEC.

To sum up, the selected flare reveals non-stationary energy release process with the three stages characterized by different efficiency of plasma heating and acceleration of electrons. Paper I was concentrated on the study of the first sub-flare as it reveals the most intensive HXR and microwave emission sources in the vicinity of the PIL, that allowed to investigate accelerated electrons and plasma heating at the PIL in details. However, in this work we investigate dynamics of the magnetic field and PVEC for the entire flare including all three sub-flares. We want to find any changes in the PVEC and photospheric magnetic field distribution in the flare region associated with the separate sub-flares.

## 2.2. COMPARISON OF X-RAY EMISSION SOURCES WITH MAGNETIC FIELD AND PVEC

The X-ray maps (Figures 2 and 3) were reconstructed with the CLEAN algorithm (Hurford et al. 2002) using the data of the RHESSI detectors 1, 3, 5, 7, and 8 for three time intervals during the first sub-flare. We do not present maps for the second and the third subflares due to the low RHESSI count rate that leads to noisy images. Figure 2 shows

the X-ray sources in two energy bands of 6–12 and 25–50 keV. The first band corresponds mostly to the thermal emission, while the second one is mostly produced by accelerated (nothermal) electrons precipitated into the chromosphere. The X-ray maps are plotted as the contours of constant levels and overlaid onto the HMI magnetic field maps. For this comparison we used the standard HMI vector magnetogram with temporal resolution of 720 s, as they are less noisy than 135-s ones. Vector magnetic field components were calculated from the reprojected onto the heliographic grid HMI vector magnetogram in the cartesian heliocentric coordinates. Vertical and horizontal magnetic field maps are shown in the top and bottom panels of Figure 2, respectively. The PIL has the S-shaped form that is typical for active regions with strong electric currents and containing sigmoids.

One can see that the SXR and HXR emission sources were generated in the region near the PIL with strong horizontal magnetic field. There were a few HXR sources. From the vertical magnetic field map one can see that the two strongest HXR sources were located close to the northern and southern magnetic islands near the PIL. In the beginning of the impulsive phase there were three HXR sources, and the SXR emission source at this time had a worm-like shape, elongated along the PIL. The SXR emission was generated from the thin channel with the approximate length of  $\approx 40''$ , filled with hot plasma. From the Paper I we also know that this worm-like emission source is also seen in the “hot” AIA channels and is associated with the strongly sheared magnetic loops. Thus, the observed EUV and SXR emissions were generated, most probably, from the magnetic loop volume in the corona. The X-ray contour maps in the subsequent two time intervals show the rather compact SXR source located between the double HXR sources. In these cases we observe the highly-sheared (about 80 degree) magnetic structure.

To reconstruct vertical PVEC density ( $j_z$ ) maps shown in the top panels of Figure 3 we applied Ampere’s law to the horizontal magnetic field components in the HMI vector

magnetogram (e.g. Guo et al. 2013; Musset et al. 2015). The ribbon-like regions of the strongest PVEC density are located near the PIL and close to the two strongest HXR sources. However, similar to the previous works there are no exact spatial correspondence, i.e. the most intense HXR pixels are not co-spatial with the pixels of the strongest PVEC density.

In the bottom panels of Figure 3 we show the absolute value of the vertical magnetic field gradient  $\nabla_h B_z = \sqrt{(\partial B_z / \partial x)^2 + (\partial B_z / \partial y)^2}$  in the local plane of the solar surface. The strongest values of  $\nabla_h B_z$  ( $\approx 1 - 2$  kG/Mm) are found along the PIL, and also concentrated in the vicinity of the two strongest HXR sources. The best coincidence between the HXR sources and the regions of the strongest  $\nabla_h B_z$  was achieved in the beginning of the flare impulsive phase. The distance between the HXR centroids and the nearest HMI pixels with the maximal PVEC density is about  $3''$  for the southern HXR source and  $5''$  for the northern one.

To resolve fine spatial structure of the flare energy release in the lower solar atmosphere and to compare them with the PVEC density maps we used Ca II (6684 Å) images from the Solar Optical Telescope (SOT: Tsuneta et al. (2008)) onboard the space solar observatory Hinode (Kosugi et al. 2007). In Figure 4 we present comparison between two  $j_z$  maps, deduced from two successive 720-second HMI vector magnetograms, and two optical cumulative images from SOT. The cumulative image is a sum of all available SOT images within the corresponding 720-second integration time interval of the corresponding HMI magnetogram. Such images present information about spatial distribution of total photospheric response during the impulsive phase and allow to compare roughly the high-cadence Hinode data with the HMI maps with low temporal resolution. One can see that the most intense optical emission was generated in the regions of enhanced PVEC density but avoid places with the strongest  $j_z$  values. In the next section we will

demonstrate temporal evolution of the PVEC in the PIL region in more details.

To sum up, the regions of the strongest PVEC density and magnetic field gradient, calculated using the 720-second HMI vector magnetograms, do not correspond exactly to the places of the most intense HXR and optical emission. However, in general, the flare emission sources are in very close vicinity ( $\approx 3 - 5$  arcsec) to the regions of enhanced PVEC.

### 3. CHANGES OF PHOTOSPHERIC MAGNETIC FIELD AND PVEC AROUND THE PIL FROM HMI VECTOR 135-SECOND MAGNETOGRAMS

In the previous section we compared the X-ray and optical images with the magnetic field maps deduced from the HMI vector magnetograms with time cadence of 720 s. This temporal resolution is insufficient to resolve magnetic field dynamics during the subflares, whose impulsive phase has typical duration of  $\approx 5$  minutes. In this section we will describe the magnetic field dynamics during the flare studied using the high-cadence HMI vector magnetograms with temporal resolution of 135 s.

The HMI 135-seconds vector magnetograms were previously described in the work of Sun et al. (2017). It was shown that the maximum of the field strength  $B$  distribution is achieved at value of 130 Gauss. This value is typical for the quiet Sun as the polarization degree is low, and the the most probable  $B$  is due to the photon noise. This noise mostly affects on the determination of the horizontal magnetic field component. We reconstructed  $B$  distribution in the quite Sun outside the active region where the flare was triggered and found the most probable value of  $B$  as 110 Gauss. This value was taken as the upper boundary for the magnetic strength error.

Let's consider magnetic flux from the region consisting of  $N$  HMI pixels. In this case

the magnetic flux error will be proportional to  $\sqrt{N}$  and thus is very small for the large-scale flare regions (since the magnetic flux is proportional to  $N$ ) even for the horizontal magnetic field component. We also used the Monte-Carlo simulation to estimate errors of calculated magnetic fluxes and found them very small. Further in the work we will not show the error bars for magnetic fluxes as they are small comparing with the size of the data points. Variations in the time-profiles for the magnetic field components and PVEC are mostly due to the limited region-of-interest (ROI) considered. We do not track the isolated magnetic flux tube. Different types of horizontal motions can lead to irregular variations for calculated fluxes inside the small ROI considered.

We should also mention that the observed dynamics of the magnetic fields and PVEC during the flare is not distorted by artifacts connected with the wrong measurements of the Fe I line. Such incorrect HMI data can be connected with sharp energy release in the lower solar atmosphere leading to distortion of the Stokes profiles of the measured line Fe I. The argument that it is not our case is the absence of fast and high amplitude variations from pixel to pixel on the magnetograms analyzed. Such variations are quite typical for strong white-light solar flares. For example, in the work of Sun et al. (2017) all 4 Stokes profiles were shown for a flare ribbon point and compared with the quiet Sun profiles. There were very strong distortions that explains magnetic field artifacts. We also checked the Stokes profiles for the selected points in the vicinity of the PIL, where the HXR, UV and optical emissions were generated. We found that the Fe I line did not reveal strong distortions, and, thus, we assume that the magnetic field is measured correctly. Therefore, PVEC is also calculated correctly.

The time sequence of the magnetic field component maps is shown in Figure 5. There are maps for the magnetic field absolute value (bottom panels), horizontal (middle panels) and vertical (top panels) components. These maps reveal that there were no significant



changes in the vertical magnetic field component when the horizontal magnetic field near the PIL was significantly intensified during the flare. Figures 6(a, b) demonstrate the time profiles of magnetic fluxes  $F_z = |B_z^{ij}|S_{pix}$  for the negative and positive vertical components, where  $ij$  superscript means summation through pixels inside a particular region and  $S_{pix}$  is the single pixel area. These fluxes were calculated in the area (shown by the black thick contour in Figure 8(a)) around the PIL with strong PVEC density. One can see that both magnetic fluxes do not reveal significant changes around the flare onset. The negative and positive fluxes have opposite trends: decreasing and increasing, respectively.

To compare real magnetic flux  $F_z$  with dynamics of the other magnetic field components through all analyzed area, we introduce nominal magnetic flux for the horizontal component ( $B_h$ ) and absolute value ( $|B|$ ) of the magnetic field. It means that we calculated the sum of magnetic field pixel values multiplied by the total area of the region considered. Figures 6(c1–c3) show temporal dynamics of magnetic flux  $B_h^{ij} S_{pix}$  for the horizontal magnetic field component. These three panels present the time profiles of fluxes calculated by summing pixels with magnetic field values higher than three thresholds: of 0, 1, and 2 kG. The relative magnetic flux change in Figure 6(c1)  $(F_{max}^h - F_{min}^h)/F_{min}^h \approx 0.4 \times 10^{21}/2.1 \times 10^{21} \approx 0.19$ , where  $F_{min}^h$  and  $F_{max}^h$  are the magnetic fluxes before the flare onset (the minimal value) and after the flare (the maximal value), respectively. The relative flux change in Figure 6(c2) is about 0.58 with  $F_{max}^h \approx 1.9 \times 10^{21}$  Mx which is 76 % from the total horizontal magnetic flux. In other words the largest fraction of the horizontal magnetic flux is contained in the strong magnetic field with  $B_h > 1000$  G. The strongest ( $B_h > 2000$  G) horizontal magnetic field appeared around the maximal SXR flux, or approximately 40 minutes after the flare onset (Figure 6(c3)).

The time profiles for the total magnetic fluxes  $|B^{ij}|S_{pix}$  ( $|B| = \sqrt{B_h^2 + B_z^2}$ ) are plotted in Figures 6(d1–d3). The fluxes shown in Figures 6(d1–d3) were calculated, as before, by

summing pixels with the magnetic field absolute values higher than three thresholds: of 0, 1, and 2 kG (as above). The change of the total magnetic flux is also associated with the flare onset. According to Figure 6(d1), the maximal total magnetic flux  $F_{max} \approx 3.2 \times 10^{21}$  Mx and the relative change is  $\approx 0.12$ . Comparing panels (c) and (d) one can conclude that the largest fraction of the total magnetic flux is contained in the horizontal magnetic field. For example comparing panels (c1) and (d1) we have  $F_{max}^h/F_{max} \approx 0.78$ , or comparing panels (c2) and (d2)  $F_{max}^h/F_{max} \approx 0.59$ . Thus, we can add that the strong ( $B_h > 1000$  G) horizontal magnetic field gives the largest contribution to the total magnetic flux.

The spatial distributions of PVEC density and horizontal gradient of vertical magnetic field are shown in Fig. 7. The top panels reveal variations in spatial structure of the PVEC density. One can notice that the region with strong PVEC density experienced slight expansion around the PIL. It can be seen for the outer contours (especially for the negative PVEC shown by red). Another peculiarity is fragmentation of the region with strong PVEC density. In the first map there was only one centroid for the negative PVEC density in the south part of the PIL. The later time instants reveal three strong intensifications. In the case of the magnetic gradient map there were no significant changes. The regions with the largest gradients experienced slight distortions.

Figure 8 demonstrates variations of the averaged characteristics of the regions with enhanced PVEC density in the PIL region (marked by the black thick contour in panel (a)) quantitatively. Three panels (from 1 to 3) in each row (c–e) show cases considering the PVEC density above three thresholds with values of  $1\sigma(j_z)$ ,  $3\sigma(j_z)$  and  $5\sigma(j_z)$ . The black and red colors in each panel of Figure 8(c–e) correspond to the positive and negative PVEC density, respectively.

To estimate the background (noise) level  $\sigma(j_z)$  for the PVEC density we calculated the  $j_z$  distribution in the non-flaring region marked by the black rectangle in the lower

right corner in Figure 8(a). This distribution is shown in Figure 8(b) by the histogram, where the solid line is a Gaussian fit and the two dashed vertical lines mark the  $1\sigma(j_z)$  level. Calculated sigma is about  $11 \text{ mA/m}^2$  which is comparable with the estimation  $\sigma_j = c\sqrt{6}\sigma_B/(16\pi\Delta x) \approx 14 \pm 4 \text{ mA/m}^2$  for  $\sigma_B \approx 110 \pm 30 \text{ Gauss}$  and pixel size  $\Delta x = 0.5''$ . Here  $c$  is the speed of light. To estimate errors in determination of total PVEC (c1–c3), area of regions (d1–d3) with the enhanced PVEC density and effective PVEC density (or, averaged PVEC density, e1–e3) we used the Monte-Carlo simulation technique. In the selected ROIs we added Gaussian noise with  $\sigma_j = 11 \text{ mA/m}^2$  to calculated  $I_z$  map and deduced all needed parameters in 100 runs. Then by calculation of standard deviations we found all needed sigmas for each time moment. Errors in panels (c1–e3) of Figure 8 are shown for three sigma levels. As one can see all small amplitude variations more-or-less are in the range of the three sigma level. However, some monotonic variations on time scale of a few 135-s frames can be due to limited ROI and connected with the photospheric motions.

Temporal dynamics of the total PVEC  $I_z$  in the PIL region is shown in panels Figure 8(c1–c3). One can see that  $I_z$  had a jump during the flare onset (the first sub-flare) and continued increasing — until around the flare SXR emission peak for  $j_z < 0$  and even further for  $j_z > 0$ . Dynamics of  $j_z$  is shown in details in Fig. 9. Considering the case  $|j_z| > 1\sigma(j_z)$  shown in Figure 8(c1), the relative value of  $I_z$  change is estimated as  $[max(I_z) - min(I_z)]/min(I_z) \approx 0.26$  for both polarities. The higher amplitudes were achieved in the cases  $|j_z| > 3\sigma(j_z)$  in Figure 8(c2) and  $|j_z| > 5\sigma(j_z)$  in Figure 8(c3): 0.41 and 0.22 (for  $j_z < 0$ ), 0.69 and 0.73 (for  $j_z > 0$ ), respectively.

Temporal dynamics of the area of the regions with the enhanced PVEC density is shown in Figure 8(d). The area was calculated as a sum of all pixels above the corresponding thresholds of  $1\sigma(j_z)$ ,  $3\sigma(j_z)$  and  $5\sigma(j_z)$ . We found changes of the area similar to  $I_z$  (increasing after the flare onset). Figures 8(d2) and (d3) revealed the largest jumps of the

area for the positive PVEC density: from 26 to 48 and from 12 to 20 Mm<sup>2</sup>, respectively. Thus, the total PVEC increased simultaneously with increasing photospheric cross-sectional area of the electric current carrying magnetic structure.

Figures 8(e) present the temporal profiles of the estimated effective PVEC density  $j_z$  in the PIL region. It is calculated as the ratio of the total PVEC  $I_z$  (Figures 8(c)) to the area (Figures 8(d)). The changes of  $j_z$  have different trend comparing with the total PVEC and area of the regions with enhanced PVEC density. One can see that there is a peak of  $j_z$  after the flare onset. This increase of  $j_z$  is especially pronounced for  $j_z < 0$  shown in Figure 8(e2) and Figure 8(e3), where  $|max(j_z)| \approx 70$  and  $\approx 105$  mA/m<sup>2</sup>, respectively. After this peak,  $j_z$  gradually decreased. We see this tendency in each panel of Figures 8(e) for both current signs except for  $j_z > 0$  in Figure 8(e1), for  $|j_z| > 1\sigma(j_z)$ , that could be due to contribution of background into  $j_z$  estimation. Zoom-in of Figures 8(c–e) is presented in Figure 9 for better clarity.

Let’s summarize the results about the magnetic field and PVEC dynamics in the entire flare energy release site. High-cadence 135-seconds HMI magnetograms reveal intensification of the horizontal magnetic field component around the PIL, where we observed the flare emission sources. Maps of the vertical magnetic field component did not show flare-related dynamics. We found that the total PVEC gradually increased during the entire flare, while the estimated PVEC density shown non-monotonic dynamics with the peak during the first subflare. Then we observed the decreasing effective PVEC density.

#### 4. 3D MAGNETIC STRUCTURE OF THE FLARE REGION

The HMI vector magnetograms allow to investigate magnetic field dynamics only on the photospheric level. To study temporal dynamics of the 3D coronal magnetic field structure

we used the NLFFF extrapolation applied to the time sequence of the HMI 135-second vector magnetograms used as the boundary condition. The magnetic field extrapolation was made using the implementation of the optimization algorithm (Wheatland et al. 2000) developed by Rudenko & Myshyakov (2009). The same procedure and extrapolation parameters are used as in Paper I (see Paper I for details). It should be noted here that the flare studied was a confined event without eruption of a filament and magnetic flux-rope. Consequently, the flare was not accompanied by destruction of the magnetic structure of the active region. This partly justifies the use of a force-free approach to describe the magnetic structure and its dynamics in a given event.

The NLFFF extrapolation results are shown in Figures 10(a) and (b), where a set of selected magnetic field lines (violet) is plotted. These field lines are started from the points in the PIL region, where the strong PVEC density (shown by the blue-red base maps) are concentrated. Figures 10(a) and (b) correspond to the very begin and peak (i.e. the SXR flux maximum) of the entire flare, respectively. At the beginning of the flare, highly sheared intersecting magnetic field lines were involved into the initial energy release process above the PIL. This magnetic configuration is favorable for the TCMR, and the compact twisted magnetic field lines observed at the flare maximum along the PIL in the form of a magnetic flux rope is a result of the magnetic restructuring due to the TCMR process (see also Paper I). It can be seen that, in general, magnetic field lines around the PIL became more pressed to the solar surface during the flare. (More detailed dynamics of the magnetic field lines in the PIL region is shown in the movie available in the supplementary materials to the paper on the journal website.)

Figures 10(c) and (d) present the 3D structure of coronal electric current density in the PIL region for the two time instants (the same as in Figures 10(a) and (b), respectively). It is shown by the white semitransparent surface corresponding to the coronal electric

current density of constant level  $55 \text{ mA/m}^2$ , which is calculated using the Ampere’s law applied to the NLFFF extrapolation results. One can see that the flare energy release lead to expansion of the worm-like current-carrying region elongated along the PIL. The pre-flare state was characterized by the thinner channel of strong electric current density. Then this channel became thicker across the PIL. Here we need to note that the NLFFF approximation gives only electric currents flowing along magnetic field lines. (Temporal evolution of the current surface is also presented in the movie which can be found in the supplementary materials to the paper on the journal website.)

The NLFFF modelling reveals the flare-related magnetic field restructuring around the PIL. We found formation of the flux-rope-like magnetic structure along the PIL and the sheared magnetic arcade and expansion of the worm-like electric current channel in the corona. It corresponds to formation of the region with the strong horizontal magnetic field component and enhancement of the total PVEC (described in the previous section).

## 5. CHANGES OF MAGNETIC FIELD AND PVEC IN THE UV FLARE RIBBONS

Flare ribbons are associated with footpoints of magnetic field lines directly connected with the magnetic reconnection site and their observation is important for diagnostic of the flare energy release process. Here we will study variations of magnetic field and PVEC density inside the fare ribbons in the PIL region. Previous researches used mostly LOS magnetograms and vector magnetograms with low temporal resolution (like 720-second HMI vector magnetograms) to study non-stationary magnetic fields in flare regions. But it is not very suitable for highly dynamic solar flares revealing three-dimensional magnetic structure. New HMI 135-second vector magnetograms allow to trace better all magnetic field components and PVEC density distribution in the moving flare ribbons.

To determine the flare ribbons we used AIA UV 1700 Å images. This UV emission is generated from the chromosphere. Temporal resolution of this data product is 24 seconds and the pixel size is  $\approx 0.6''$ . In each image area of the flare ribbons is calculated as a sum of pixels with intensity values higher than the threshold value of 3800 DN. Figure 11 presents temporal sequence of binary maps (the black-white background images) showing the flare ribbon positions deduced from AIA UV 1700 Å images. Each pixel in these maps can have value of 0 or 1. Value 1 means that this pixel is inside the flare ribbons. Positions of the flare ribbons are compared with the regions of strong PVEC density shown by the red and blue contours corresponding to the negative and positive PVEC density, respectively. The brightest flare ribbons are close to the strongest PVEC density intensifications qualitatively. However, there is no exact correspondence. The distant southern and northern UV sources do not have corresponding strong PVEC density. The bottom panels reveal small (a few arcseconds) displacement of the flare ribbons from the PIL and appearance of corresponding PVEC density intensifications. Thus, dynamics of the flare ribbons and regions with enhanced PVEC density are in qualitative matching with each other.

In Figure 12 the temporal profiles of the flare ribbon area (a) and total UV intensity (b) are shown by the black histograms and compared with the GOES 1–8 Å lightcurve (cyan) and its time derivative (blue). The time axis is also (as in Figure 1) on a logarithmic scale to show the impulsive phases of three sub-flares in more details. The fastest intensity growth and maximal value was during the first sub-flare with the largest area change of  $\approx 1.3 \times 10^{18} \text{ cm}^2/\text{s}$ . The maximal ribbon area is about  $1.4 \times 10^{18} \text{ cm}^2$ .

The sequence of the UV images reveals sharp enhancement of the ribbon area during the first frames (Figure 12) of the first subflare. Dynamics of the ribbons linear size scales can be splitted into two phases. The first one is not very evident as we do not have sufficient temporal resolution. However, comparing the first and the second images (two left top

images) one can see the ribbons expansion or elongation along the PIL from the initial brightenings. The second stage is characterized by the gradual ribbons separation out from the PIL.

To investigate details of the ribbons evolution during the first stage we present Figure 13 with six (non-binary) UV images compared with PVEC density contour maps. Initially (panel a) we observe small weak emission sources in the regions of strong PVEC density. Then in panel b, we see the large scale ribbons with non-uniform brightness distribution from -245 up to -175 arcseconds along the south-north direction. This expansion occurred on the 24-seconds time scale of temporal resolution for AIA UV 1700 Å images. This elongation could be due to real expansion of the separate emission sources along the PIL or appearance of the sequence (chain) of new sources along the PIL. Despite on this uncertainty, further in the text the increase of the ribbons area during the first 24 seconds of the first subflare will be referred as the ribbons elongation along the PIL. In other words, we want to say that magnetic flux change inside the flare ribbons was due to process of energy release spreading along the PIL. One can see (panels (c)-(f)) that later the length of the flare ribbon did not vary very much, while the ribbon emission intensity varied with time.

The initial ribbon separation was about 1 Mm. Considering the whole event, the averaged ribbon velocity ( $V_{rib}$ ) in the perpendicular direction to the PIL is  $\approx 5''$  per 10 minutes or  $V_{\perp} \approx 6.25$  km/s. To estimate expansion rate  $V_{\perp}$  during the very beginning of the impulsive phase (the upper limit) let's assume fast expansion of the flare ribbon up to its width from the initial brightenings. In this case, the velocity is  $\approx 3''$  during 24 seconds (the time cadence of AIA 1700 Å images), or  $V_{\perp} \approx 100$  km/s.

The parallel velocity  $V_{\parallel}$  of the ribbon elongation during the first subflare cannot be measured directly, because of its fast elongation time relatively to the AIA 1700 Å cadence



(24 s). However, we can estimate it by the following way. Considering ribbons width  $V_{\perp}t$  much smaller than its length  $V_{\parallel}t$  the total area  $S(t)$  of both flare ribbons can be approximated as  $S(t) = 2V_{\parallel}V_{\perp}t^2$  and the expansion rate is  $dS/dt = 4V_{\parallel}V_{\perp}t$ . Considering the first sub-flare, one can estimate the elongation velocity as  $V_{\parallel} = \Delta S/(4V_{\perp}\Delta t^2) \approx 560$  km/s for the beginning of the impulsive phase taking  $\Delta t = 24$  seconds,  $\Delta S \approx 1.3 \times 10^{18}$  cm<sup>2</sup> and  $V_{\perp} \approx 100$  km/s. As we considered the maximal possible value of  $V_{\perp}$  the obtained  $V_{\parallel}$  is the lower limit. If we will take smaller  $\Delta t$  than velocity will be larger up to the Alfven velocity  $V_A \approx 6900$  km/s considering  $B = 1000$  Gauss and ion density of  $n_i = 10^{11}$  cm<sup>-3</sup> (see Paper I). For  $v_{\parallel} = v_A$  the ribbons elongation developed on the time scale  $\Delta t \approx 0.5$  s. To sum up, one can say that  $V_{\parallel} \gg V_{\perp}$  during the beginning of the impulsive phase. Than the flare ribbon elongation was finished and we observed their slow motion out from the PIL. This picture is quite similar to the two step reconnection process discussed in (e.g. Qiu et al. 2010; Priest & Longcope 2017).

To calculate the magnetic field parameters inside the flare ribbons at the time of the selected AIA UV 24-second frame we used linear interpolation between corresponding pixels of two neighboring HMI 135-second magnetograms (the UV frame is between these two magnetograms). Time derivatives of the magnetic (vertical component) flux inside the flare ribbons is shown in Figure 14(a) by the black (negative) and red (positive) histograms. Such time derivative is usually referred as the magnetic reconnection rate. One can see that the largest reconnection rate of  $\approx 7 \times 10^{18}$  Mx/s was achieved in the beginning of the impulsive phase. This reconnection rate is almost two times larger than for the second sub-flare. It is also worth noting that two enhancements of the reconnection rate during the second sub-flare are in accordance with two major heating bursts deduced from the time derivative of the GOES SXR lightcurve.

Figures 14(b) and (c) present variations of the magnetic field components inside the

flare ribbons. Panel (b) demonstrates magnetic flux (orange) around the PIL, which is calculated using the vertical magnetic field component. This panel also demonstrates nominal magnetic fluxes deduced for the absolute value of the magnetic field (black) and for the horizontal magnetic field component (red). This nominal magnetic flux is introduced to make comparison between the magnetic field components over all ribbons area. The time profiles of the magnetic field components averaged over the flare ribbon area are plotted in panel (c) with the same meaning of colors as in panel (b). Each sub-flare was characterized by approximately the same enhancement of the total magnetic flux with the magnitude of  $\approx 6.5 \times 10^{19}$  Mx. The first and second sub-flares were characterized by the averaged absolute magnetic field value of  $\approx 1100$  G, when the third one had slightly less value of  $\approx 800$  G. However, the main result is that the magnetic field inside the flare ribbons associated with the first sub-flare were more horizontal than in the case of the subsequent sub-flares. At the time of the maximal  $|\vec{B}|$  during the first sub-flare the ratio  $\langle B_h \rangle / \langle B_z \rangle \approx 1.62$  and the flux ratio was about 1.66. For the second and third sub-flares these ratios had the following values: 1.3 and 1.2, and 1.2 and 1.1, respectively.

Figure 15 shows the following time profiles: (a) the total PVEC inside the flare ribbons, calculated as a sum of pixel values above  $35 \text{ mA/m}^2 \approx 3\sigma(j_z)$ ; (b) the effective (or averaged) PVEC density inside the flare ribbons estimated as the ratio of the total PVEC (panel (a)) to its area, whose time profile is shown in panel (c). The time profiles are shown for the positive (red) and negative (black) PVEC density signs. Despite of the large area of the flare ribbons during the third sub-flare, one can see that the total PVEC was small comparing with the first and second sub-flares having  $I_z \approx 4 - 5 \times 10^{11}$  A for the positive and negative signs. Maximal effective PVEC density was about  $60 \text{ mA/m}^2$  for the first and second bursts. The flare ribbons were partially covered by the regions with strong PVEC density. From panel (c), the maximal area of the regions with strong ( $> 35 \text{ mA/m}^2$ ) PVEC density was  $\approx 10^{17} \text{ cm}^2$ , which is about 10 % from the total area of the flare ribbons. From

Figure 15(b) we can make an important conclusion that the temporal variations of plasma heating and electron acceleration efficiency (inferred from the time derivative of the SXR lightcurve and the Neupert effect) is consistent, in general, with the variations of effective PVEC density inside the flare ribbons.

The analysis done in this section allowed us to make detailed comparison of the flare energy release with the changes of the magnetic field and PVEC in the flare ribbons, connected with the energy release site. We found good time consistency of the flare energy release efficiency (approximated by the time derivative of the GOES lightcurve) with the magnetic reconnection rate and total PVEC inside the ribbons.

## 6. DISCUSSION

### 6.1. MAIN RESULTS

Using the new HMI vector magnetograms with the high time cadence of 135 s, we investigated dynamics of the photospheric magnetic field and PVEC in the PIL region during the three successive subflares of the confined M1.2 class solar flare on 2015 March 15 (SOL2015-03-15T22:43), previously studied in Paper I (Sharykin et al. 2018). The following main data analysis results were obtained:

- The flare X-ray sources, as well as the optical and UV flare ribbons, were located in the regions of the strong horizontal photospheric magnetic field, PVEC density and the horizontal gradient of the vertical magnetic field component on the photosphere. However, there was no exact spatial matching between the most intense pixels of the HXR images and the maps of PVEC density and magnetic field gradients (the displacement is around 3-5 arcseconds).

- The photospheric magnetic field was mostly horizontal near the PIL region. The magnetic field became more horizontal during the flare. The largest fraction of the magnetic flux was concentrated in the strong ( $B > 1000$  G) magnetic field. There were no fast changes of the vertical magnetic field component of both polarities.
- The total PVEC near the PIL region increased simultaneously with the increasing photospheric cross-sectional area of the current-carrying magnetic structure. The effective PVEC density first increased impulsively with the flare onset and then decreased gradually with the flare development. Expansion of the regions with the strong PVEC is in qualitative accordance with the motion of the flare ribbons from the PIL.
- The first sub-flare accompanying by the efficient (with the hardest spectrum) electron acceleration and the strongest heating was associated with the largest changes of the magnetic flux in the flare ribbons. During the flare development the flare ribbons penetrated into the regions with more vertical magnetic field, while they were initially characterized by the dominant horizontal magnetic component. The expansion of the flare ribbons was characterized by enhancement of the total PVEC and effective PVEC density inside them, which had tendency to coincide temporally with the lightcurves of microwave emission and time derivative of the SXR lightcurve.
- The NLFFF extrapolation based on the HMI high-cadence vector magnetograms revealed fast changes of the magnetic field structure in the PIL's vicinity. It was found that magnetic field lines started from the regions of strong PVEC became shorter, in general, and formed the low-lying magnetic flux-rope-like structure embedded in the sheared magnetic arcade along the PIL at the end of the flare energy release process. The pre-flare state was characterized by the highly sheared magnetic structure intersecting above the PIL that is favorable for the TCMR.

In the following subsections we will discuss these observational phenomena jointly with the results from Paper I in the context of the TCMR above the photospheric PIL. We will try to give qualitative interpretation of the phenomena observed during the flare and make the order of magnitude estimations of some important physical parameters related to the energy release processes. The energetics and efficiency of the magnetic reconnection, filamentation of energy release site, dynamics of the magnetic fields and electric currents, acceleration of electrons will be discussed in the separate subsections.

## 6.2. MAGNETIC RECONNECTION IN THE PIL REGION

In this work we considered the confined solar flare without a fully-developed eruption and CME. Analysis of the magnetic field extrapolation results and morphology of the emission sources in the various ranges of the electromagnetic spectrum revealed that the flare energy release was developed in the low lying magnetic field structure elongated along the PIL. The presence of the sheared core magnetic structure with crossed magnetic field lines above the PIL is in favor of interaction of the magnetic flux tubes (loops) in the frame of the TCMR scenario (Moore & Roumeliotis 1992; Moore et al. 2001). This process is characterized by strong longitudinal (guide) component of the magnetic field in a reconnecting current sheet. Photospheric vector magnetograms revealed that the flare ribbons were localized in the strong magnetic field with the dominating horizontal component. Most possibly, the flare energy release was triggered in the localized magnetic field shear layer above the PIL. In this section we will discuss this 3D magnetic reconnection as the source of energy release of the flare studied. We will perform some basic estimations to derive the main physical characteristics of the reconnection process.

Firstly, we will list the main characteristics of the energy release process (associated with the magnetic reconnection) found from the observations and NLFFF extrapolations of

the magnetic field described in Paper I and in this work:

1. There were no apparent plasma ejection, eruption, and CME during the flare; the flare was highly confined;
2. Reconnected magnetic fields swept the regions with strong PVEC, thus, the magnetic reconnection occurred in the twisted/sheared magnetic structure;
3. The most favorable magnetic configuration for magnetic reconnection was the tether-cutting geometry, where the crossed magnetic loops with the high shear (up to  $80^\circ$ ) interacted with each other above the PIL forming a current layer with the strong longitudinal magnetic field component with the average value of  $B \approx 1000$  Gauss;
4. During the beginning of the flare impulsive phase we observed very fast expansion of the emission sources along the PIL with the velocity lying in the range of  $\approx 600$  km/s up to the Alfvén velocity of  $\approx 7000$  km/s. Then, there was more gradual slow separation of the ribbons with velocity  $\lesssim 10$  km/s quasi-perpendicular to the PIL. One can assume the two-step flare energy release process;
5. The flare onset was accompanied by the impulsive increase of the average PVEC density in the PIL region;
6. In general, the flare process was accompanied by simultaneous increase of the total PVEC and decrease of the average PVEC density in the entire flare region, while the total PVEC and average PVEC density in the flare ribbons correlated with non-thermal flare emission;
7. The magnetic reconnection rate had the maximum value of  $\approx 7 \times 10^{18}$  Mx/s during the time period of the most efficient electron acceleration during the first sub-flare;

8. Electron acceleration was accompanied by plasma heating up to the super hot temperatures  $T \approx 40$  MK;
9. Accelerated electrons and hot plasma were localized in the thin magnetic channel with the width of  $\sim 0.5$  Mm and length up to 10 Mm. Thus, the efficient confinement of the thermal and nonthermal electron populations was observed in directions transverse to the PIL.

These characteristics are the base for the further discussion of the energy release process in the flare studied.

In Figure 16 we present the proposed geometry of the magnetic reconnection region in the frame of the TCMR scenario (panel (a)). The geometric sizes and magnetic structure of the reconnection site are shown in panel (b). The basic parameter of the magnetic reconnection is the reconnection rate  $d\phi/dt$ , defined as a time derivative of magnetic flux through the flare ribbons (e.g. Forbes & Lin 2000). This magnetic flux determines magnetic inflow into a current sheet where magnetic reconnection develops. The reconnection rate is proportional to the electric field  $E$  in the reconnecting current sheet:  $d\phi/dt \sim cEL$ , where  $c$  is the speed of light,  $L$  is the length scale of the current sheet. We found the maximal value  $d\phi/dt \approx 7 \times 10^{18}$  Mx/s and, thus,  $E \sim 2/L$  statvolt/cm inside the current sheet with  $L$  in Mm. Using the results of the Paper I one can take  $L \sim 1$  Mm, which is the width of the hot channel at the PIL seen in the “hot” EUV bands (AIA/SDO 94 and 131 Å; see Figure 17). The magnetic reconnection rate is also can be calculated as  $d\phi/dt \sim v_{in}gB_{in}L$ , where  $v_{in}$  is velocity of plasma flowing into the current sheet with the length scale  $L$ , and  $g$  is a geometric factor connected with magnetic shear across the current sheet (Fig. 16b). It means that the parallel electric field along the sheet is connected with  $gB_{in}$  at the current sheet boundaries. It is difficult to estimate  $g$  from observations, and we just assume that it is less than unity. It is also difficult to estimate the current sheet length

$L$ . One could assume  $L \sim l$ , where  $l$  is the current sheet height in the vertical direction out from the photosphere and it is about 1 Mm (i.e. a cross section size of the flare loop; see Paper I). However, it seems that due to the high shear,  $L$  should be a few times larger than  $l$ . For further estimations let's take in mind that  $gL \sim 1$ , for  $L$  described in Mm. But, not to loss generality, this factor will be written in the following expressions. One can find  $v_{in} \approx 700/(gL_{[Mm]})$  km/s, and the dimensionless reconnection rate (i.e. the Alfven Mach number in the inflow region)  $M_A = v_{in}/v_A \approx 0.1/(gL_{[Mm]})$  for the Alfven velocity  $v_A = 6900$  km/s considering  $B = 1000$  G and ion density of  $10^{11}$  cm $^{-3}$ . The estimated value of  $M_A$  is close to the upper limit of the magnetic reconnection rate found in other works (e.g. Yokoyama et al. 2001; Isobe et al. 2005; Lin et al. 2005; Narukage & Shibata 2006; Takasao et al. 2012; Su et al. 2013; Nishizuka et al. 2015; Cheng et al. 2018). However, these works considered the flares in the frame of the “standard” model. The characteristic velocities were in the range of 10 – 100 km/s that is significantly smaller relative to our estimation of  $v_{in} \approx 700/(gL_{[Mm]})$  km/s.

It seems that the estimated inflow velocity is too large. For example, considering even 100 km/s one has a displacement of magnetic field lines equal to 10 Mm during the impulsive phase with the duration of 100 s. We did not observe such displacements of magnetic elements in the flare region. In the case of an eruptive flare the magnetic reconnection is triggered in a quasi-vertical current sheet stretched by a magnetic flux rope (plasmoid) moving upwards with large velocity up to  $\sim 1000$  km/s. It leads to stretching magnetic field lines below the plasmoid body and causes formation of an X-point with large inflow velocities. However, in the case of the confined flare studied here neither eruption nor plasma ejection was observed. The flare trigger can be only a slight motion of the sheared magnetic loop footpoints due to the photospheric flows in the vicinity of the PIL. Time sequence of vector magnetograms, UV and EUV images did not reveal fast motions with velocities higher than 100 km/s. From our point of view, it is unlikely that the driver of the



flare energy release in this non-eruptive flare was the large scale displacement of magnetic loops with this velocity. Possibly, such velocity could arise locally within the current sheet due to motion of the separate magnetic elements across the current sheet. For example, formation of magnetic islands (their three-dimensional analog), their relative motion and acceleration up to the Alfvén velocity within the current layer can lead to subsequent acceleration of magnetized plasma incoming to the space between magnetic islands (e.g. plasmoid induced magnetic reconnection, Shibata & Tanuma 2001).

Additional reason for the fast moving magnetic elements in the current sheet triggering intensive plasma inflow is the fast bidirectional elongation of the flare ribbons with the estimated velocity up to  $v_A$ . In the frame of the TCMR geometry two sheared magnetic loops lead to formation of a current sheet with the guide magnetic field. This current sheet at the higher heights involves into collision of higher magnetic loops having more distant footpoints comparing with the lower magnetic loops. Thus, elongation of the ribbons means involvement of magnetic field lines at higher heights. Naturally, this involvement could be very fast and determined by the Alfvén velocity, which is  $v_A \approx 6900$  km/s in the flare region studied. Usually, however, characteristic velocities of apparent HXR sources motions along the PIL are in the range of  $\sim 10 - 100$  km/s (e.g. Grigis & Benz 2005; Kuznetsov et al. 2016). Another possibility of the ribbon elongation is associated with the so-called zipping reconnection (Priest & Longcope 2017; Threlfall et al. 2018).

When elongation of the ribbons stopped, we observed gradual separation of the ribbons out of the PIL with velocity not exceeding 10 km/s. As it was shown, the magnetic field in the ribbons became more vertical during the subsequent two sub-flares. From our point of view, we observed the second-step (Fig. 18b,c) of the flare energy release. It seems that due to the TCMR process some of the reconnected magnetic field lines at the PIL moved in the vertical direction and interacted with the less sheared magnetic loops located above.

These subsequent reconnection episodes, probably produced in the magnetic tangential discontinuity layers, were observed indirectly as the slowly separated flare ribbons tracing the reconnected magnetic flux.

To estimate the current sheet width  $\delta$  one can use the continuity equation for the steady state (it is reasonable for the reconnection rate maxima when we have  $d^2\phi/dt^2 \sim 0$ ):

$$v_{in}n_{in}l = v_An_0\delta \quad (1)$$

Thus,  $\delta = l(n_{in}/n_0)M_A$  is determined by the plasma compression ratio  $n_{in}/n_0$  and dimensionless reconnection rate  $M_A$ . From our estimations  $M_A \approx 0.1/(gL)$ . To estimate the compression ratio one can assume an incompressible limit as the simplest case. Another option is to assume strong compression from the initial (background) coronal density  $n_{in} \sim 10^9 \text{ cm}^{-3}$  to the flare super-hot plasma density  $n_0 \approx 10^{11} \text{ cm}^{-3}$  (see Paper I). As a result, we obtain  $\delta \sim (10^{-3} - 10^{-1})/(gL) \text{ Mm}$ .

Another important characteristics of magnetic reconnection process is ratio  $\lambda_{mfp}/L$ , where  $\lambda_{mfp}$  is the plasma collisional mean free path and  $L$  is the characteristic length scale (in our case we assume it to be of the current sheet size). Our estimations show that  $\lambda_{mfp} \approx 0.5 \text{ Mm}$  for the super-hot plasma temperature  $T = 40 \text{ MK}$  and density  $n \approx 10^{11} \text{ cm}^{-3}$ . Thus, we have collisionless conditions taking the current sheet width  $\delta \sim (10^{-3} - 10^{-1})/(gL) \text{ Mm}$  and height  $l \sim 0.5 \text{ Mm}$ . However, for electrons propagating along the current we can consider regime of a few collisions as  $\lambda_{mfp}/L = \lambda_{mfp}g/l \gtrsim 1$ . It is likely that the magnetic reconnection process was collisionless due to the high plasma temperature.

Let's discuss briefly the flare energetics. One can estimate the energy release rate in the current sheet with the height of  $l = 1 \text{ Mm}$  (the width of the “hot” EUV channel, see

Paper I for details) and incoming magnetic field  $B_{in} = 1000$  G using the formula:

$$\frac{dE}{dt} = 2 \frac{g B_{in}^2}{4\pi} v_{in} L l = \frac{g B_{in} l}{2\pi} \cdot \frac{d\phi}{dt} \sim 10^{29} g,$$

ergs/s.

To estimate the inflow energy we neglected the kinetic and thermal energy as the magnetic energy is dominant. One can see that during the impulsive phase of the first sub-flare of duration  $\Delta t \approx 100$  s the total magnetic energy release is  $(dE/dt)\Delta t \sim 10^{31} g L$  ergs that is one order of magnitude larger than the nonthermal particle energy and a few times smaller than the change of the free magnetic energy  $\approx 2.9 - 4.6 \times 10^{31}$  ergs bearing in mind that  $gL \sim 1$  (see Paper I). Thus, the found reconnection rate, the linear scale of the current sheet and the magnetic field in the inflow region agree well in terms of the energetics.

To sum up, despite the fact that the magnetic reconnection during the studied flare has quite high rate (up to  $d\phi/dt \approx 7 \times 10^{18}$  Mx/s), its dimensionless value ( $M_A \approx 0.1/(gL)$ ) is comparable with the upper limit found in other works, where the current sheets located higher in the corona in eruptive events have been considered.

### 6.3. CURRENT SHEET FILAMENTATION AND CONFINEMENT OF THERMAL AND NONTHERMAL ELECTRONS

As we discussed above, the fast inflow velocity ( $v_{in} \approx 700/(gL)$  km/s) leading to the large reconnection rate is probably not resulted from the fast global (on the flare region scale) motions. It is likely to be connected with some local processes around the current sheet. Thus, to trigger the fast magnetic reconnection one need to assume the current sheet achieving unstable conditions somehow. This type of magnetic reconnection is usually referred as spontaneous. In the case of spontaneous reconnection, it is necessary that the current sheet is formed and accumulated sufficient amount of energy to be released during

a flare.

In Figure 17(b) we present the time-distance plot for the observational slit (the white horizontal line in panel (a)) with the AIA 94 Å image for one time instant  $\approx 20$  min before the flare onset) crossing the bright EUV channel at the PIL. One can see that the energy release in the “hot” warm-like channel along the PIL was observed long before the flare impulsive phase onset (at least before 45 min in Figure 17(b)). A similar picture was previously observed before many flares (Cheng et al. 2017, and references therein). Sudden enhancements of the channel brightness were detected episodically in the pre-impulsive flare phase. The flare initiation was preceded by the gradual increase of the EUV luminosity for  $\approx 10$  min. It seems that the energy release site was already prepared for the flare onset, and once it reached some special conditions for an instability the flare started. One can state that the current sheet could exist in the quasi-stationary state and the magnetic reconnection was slow, then the reconnection rate started to grow suddenly, which led to the beginning of the flare and its development.

It is difficult to discuss a reason for spontaneous equilibrium loss of the current sheet because of the limited capabilities of the available observational data. However, one of the possible ways to trigger transition from slow to fast regime of reconnection is to assume the tearing instability leading to formation of current filamentation inside the current sheet. The reason to consider this scenario is the fact that the accelerated electrons and hot plasma were localized in the thin magnetic filament (described in Paper I). One can assume that such filament is a bundle of magnetic flux tubes formed due to the tearing instability inside a non-neutralized current sheet. It was shown (e.g. Kliem 1994) that magnetic islands (filaments in 3D) in the current sheet can lead to efficient trapping of electrons inside the filaments.

As we know from the classical theory, the characteristic time  $\tau_{tear}$  of the tearing

instability is the shortest for large scale perturbations with  $k\delta \sim 1$  ( $k$  is the wavenumber of perturbation). This time can be estimated as  $\sqrt{\tau_d \tau_A}$  (e.g. subsection 10.2.1 in Aschwanden 2004), where  $\tau_A$  is the Alfvén time and  $\tau_d = \delta^2/\mu$  is the diffusion time across a current sheet with width  $\delta$  and magnetic diffusivity  $\mu = c^2/(4\pi\sigma)$ , where  $\sigma$  is the electrical conductivity. Considering  $\delta \sim (10^{-3} - 10^{-1})/(gL)$  Mm (estimated above), one can deduce  $\sigma_{eff} = (\tau_{tear}c)^2 v_A/(\delta^3 4\pi) \sim (2.5 \times 10^{11} - 2.5 \times 10^{17})(gL)^3$ , when the classic electrical conductivity is  $\sigma_{Sp} \approx 4.8 \times 10^{17}$  for  $T = 40$  MK. Thus, even the classical conductivity could explain formation of magnetic islands in the more narrow current sheet. But in the case of a thicker current sheet one should consider the suppressed (anomalous) electrical conductivity which can be five orders less than classical one. The electric conductivity reduction can arise due to the presence of turbulence.

Another reason to suggest the presence of anomalous transport connected with turbulence is appearance of the super-hot plasma (for details see Paper I). There are two ways to form region with the confined super-hot plasma on a time scale of the impulsive phase: 1) to organize slow heat losses from the heated region, or 2) to trigger a lot of subsequent heating events to compensate fast heat losses. Let's estimate characteristic cooling time via heat conduction as  $\tau_{cond} \approx 4nk_B L^2/(kT^{5/2}) \approx 0.13$  s for  $L = 5$  Mm (half length of 10 Mm magnetic loop) and  $T = 40$  MK. Here  $k_B$  is the Boltzmann constant and  $k$  is the thermal Spitzer conductivity coefficient. If we will consider saturation limit of heat conduction, when electrons with their thermal velocity transfer energy, one can find  $\tau_{cond} \sim 1.5V_{Te}L \approx 0.2$  s, where  $V_{Te}$  is the velocity of thermal electrons. The values obtained are too small. However, one can assume suppressed heat transfer associated with the turbulence. One need to suppress the heat conduction coefficient by four orders to achieve cooling time  $\sim 100$  s. Thus, appearance of the super-hot plasma and initiating tearing instability on the considered time and spatial scales can be possibly a result of appearance of plasma turbulence which can be triggered by different ways like strong electric current

in the magnetic structure. For example, small displacement of magnetic loops due to shear or rotational motions of their footpoints can trigger initial slow inflow ( $v$ ) to the current sheet and induce electric current  $j = \sigma_{eff}E = \sigma_{eff}vB/c$ . If this electric current exceeds particular value, one type of turbulence can start to grow. It will lead to efficient reduction of conductivity and trigger the fast magnetic reconnection due to the tearing instability accompanied by formation of magnetic filaments.

However, there is an additional reason to explain the low electrical conductivity leading to the slowly developing tearing instability. As we know from the NLFFF extrapolations the flare magnetic loops were located at very low heights  $\lesssim 3$  Mm. Thus, we can suspect that the flare energy release could be triggered at high chromospheric layers where the electrical conductivity is low and can be also suppressed by some kind of turbulence. For the chromospheric layers  $\sigma_{Sp} \approx 1.9 - 15 \times 10^{12}$  for  $T = 1 - 4 \times 10^4$  K. Possibly, instability could be triggered at the heights where electrical conductivity is low and than disturbance spread with the characteristic Alfvén velocity and involved the whole volume of the magnetic loops into the energy release process. Such picture assumes formation of the current sheet at the conditions of partial plasma ionization and high plasma density. The physics of such magnetic reconnection is quite complex and not totally understood. That's why it is difficult to discuss the chromospheric reconnection in details in the frame of the flare studied.

#### 6.4. DYNAMICS OF MAGNETIC FIELD AND ELECTRIC CURRENTS IN THE FLARE REGION

In this Section we discuss dynamics of the photospheric magnetic field components and PVEC (see the second and third items in the list of the main results in Sec. 6.1) in the vicinity of the PIL where the flare energy release developed in the conditions

of three-dimensional restructuring of the magnetic field lines within the found sheared magnetic structure. Using the HMI 135-second vector magnetograms we found the increase of the horizontal magnetic component near the PIL during the flare. This phenomenon can be explained in the frame of the TCMR scenario. The sheared magnetic loops interact and reconnect above the PIL, which results in formation of a small magnetic arcade moving/collapsing towards the photosphere. Thus, we observe the growth of the horizontal magnetic component near the PIL during the flare.

Larger scale magnetic field lines are also formed due to this reconnection process. These field lines can move upwards and interact with the overlying magnetic field above the primary energy release site. It can trigger subsequent episodes of magnetic reconnection. We observe it as the small displacement of the flare ribbons out from the PIL and appearance of the hot sheared magnetic arcade in the region with more vertical magnetic field. This expansion of the flare arcade is clearly seen in Figure 17(b), and it is associated with the separating flare ribbons. One can note that the velocity of this expansion is rather small that is in agreement with the “slipping” reconnection in the confined flares (Hinterreiter et al. 2018). Eruptions usually lead to the larger apparent velocities of the flare ribbon separation. The expansion is a result of involvement of new magnetic loops lying above the already reconnected ones. The reconnection happens between higher and higher, more distant magnetic loops from the PIL, which are less sheared and in a more potential state (Priest & Longcope 2017; Qiu et al. 2017). If a full eruption does not occur, then this process stops at some point (at some height). Determining the reason for stopping this process and a lack of developed eruption in the flare studied is beyond the scope of this work (see, e.g., Amari et al. 2018).

Let’s now discuss the observed dynamics of PVEC. It was shown that the flare impulsive phase onset was accompanied by the pulse (see Figure 8(e1–e3)) of the average

PVEC density in the PIL region, whereas, in general, the flare was accompanied by simultaneous increase of the total PVEC and gradual decrease (after the initial pulse) of the average PVEC density in the entire PIL region. Below we will try to give qualitative interpretation of the phenomenon observed.

The most detailed investigation of the PVEC dynamics comparing with the MHD numerical modeling was made by Janvier et al. (2014) for the famous eruptive X-class flare on 2011 February 15. They found an increase of the total PVEC in the regions with enhanced PVEC density during the flare. A similar effect was found for another eruptive X-class flare on 2011 September 6 (Janvier et al. 2016). However, the basic understanding tells us that flares should be accompanied by decreasing PVEC density due to release of a free magnetic energy, magnetic field relaxation to a more potential state, and loss of magnetic twist due to erupting process (magnetic helicity conservation). Janvier et al. (2014) and Janvier et al. (2016) discussed this apparent contradiction and argued that the total PVEC enhancement is associated with development of new currents during the eruption, and these new current systems, probably related to the quasi-separatrix layers QSLs, appear to match the flare ribbons in the chromosphere (see also Schmieder & Aulanier 2018, for discussions).

We need to mention that the observed dynamics is not related to the projection effect. The thing is that the observed enhancement of the total PVEC in the flare region could be connected with the magnetic field verticalization near the PIL. However, as we discussed above, the magnetic field near the PIL became more horizontal in course of the flare. Thus, the increase in the vertical current on the photosphere could not be a result of a restructuring of the magnetic field at the foot of the flare loops. Our working hypothesis is that the changes of the PVEC density distribution could be connected with electric current generation/amplification in the current sheet(s) above the PIL in course



of the TCMR. Indeed, in contrast to the 2D “standard” model, in the 3D magnetic configuration, the current flowing in the coronal current sheet(s) must be closed somewhere. We assume that this may take place, at least partially, under the photosphere. Thus, the appearance/amplification of the current in the corona can be accompanied, possibly with some delays (see below), by the appearance/amplification of vertical currents on the photosphere.

As we discussed above, the magnetic reconnection in the flare studied is a complex non-stationary process involving different magnetic loops of various spatial scales. To analyze dynamics of electric current in the current sheet qualitatively, firstly, let’s consider a single reconnection episode and try to understand the situation when we have a pulse of electric current density and gradual increase of total electric current. For simplicity, we will consider a standard rectangular diffusion region with height  $l$  and width  $\delta$  (Fig. 16b). Magnetic field at the boundaries of this region has three components: guide ( $B_{||}$ ; along the PIL), perpendicular ( $B_{\perp} = gB_{in}$ ; i.e. vertical), and transverse  $B_x$  (i.e. across the sheet) components. To estimate value of total electric current through the current sheet we use the Ampere’s law in the integral form:

$$J_{||} = \int_{S_C} j_{||} dS = \frac{c}{4\pi} \oint_C \vec{B} \cdot \vec{ds} = \frac{c}{2\pi} B_{\perp} l \left[ 1 + \frac{B_x}{B_{\perp}} \frac{\delta}{l} \right] \approx \frac{c}{2\pi} B_{\perp} l$$

Here  $S_C = \delta l$  is a cross-sectional area of the current sheet and  $C$  means the contour marking the boundary of this area. This approximate formula for  $J_{||}$  is derived assuming  $B_x \delta / B_{\perp} l \ll 1$  that is quite natural considering magnetic flux conservation  $v_{in} B_{\perp} = v_A B_x$ . Thus,  $j_{||} \propto B_{\perp} / \delta$  and  $J_{||} \propto B_{\perp} l$ . Time derivatives of the electric current density and total electric current are  $j_{||t} \propto B_{\perp t} / \delta - B_{\perp} \delta_t / \delta^2$  and  $J_{||t} \propto l B_{\perp t} + B_{\perp} l_t$ , respectively, where subscript  $t$  means time derivative. Thus, to achieve  $j_{||t} > 0$  and  $J_{||t} > 0$  one has to guarantee simultaneous fulfillment of the following conditions:  $B_{\perp t} / B_{\perp} > \delta_t / \delta$  and  $B_{\perp t} / B_{\perp} > -l_t / l$ . In other words, relative growth rate of the magnetic field near the diffusion region boundary

should be larger than change of the current sheet width and the change of the length with opposite sign. The obvious way to fulfill these inequalities is to assume the current sheet thinning, elongation and enhancement of  $B_{\perp}$  value at the reconnection region boundary. Such dynamics of a current sheet was simulated for eruptive solar flares and discussed by Janvier et al. (2016), however, one could assume the similar behavior for the three dimensional magnetic reconnection with a guide field in the closed magnetic configuration like in the frame of the TCMR scenario considered here. To achieve  $B_{\perp t} > 0$  one can consider induction equation  $B_{\perp t} = [v_{in} B_{\parallel}]_x > 0$ . It means that inflow across the current sheet leads to enhancement of the perpendicular magnetic field.

After the pulse of  $\langle j_z \rangle$ , we observed the situation when the total electric current and current density show different trends:  $j_{\parallel t} < 0$  and  $J_{\parallel t} > 0$  (see Figure 8(e1–e3)). It can be described by the following inequalities:  $B_{\perp t}/B_{\perp} < \delta_t/\delta$  and  $B_{\perp t}/B_{\perp} > -l_t/l$ . From our point of view, the most reliable and simple scenario explaining these inequalities is the magnetic annihilation process without magnetic advection described by the simple equation for the diffusion region:  $B_{\perp t} = \mu B_{\perp xx}$ , where  $\mu$  is the magnetic diffusivity and  $xx$  means double  $x$  derivative. Considering  $B_{\perp t} \approx 0$  at the boundary as there is no advection we will obtain  $\delta_t \propto \sqrt{\mu/t} > 0$  and  $j_{\parallel t} < 0$ .

We discussed the observed dynamics of  $j_{\parallel}$  and  $J_{\parallel}$  in the frame of a single reconnection episode. But enhancement of  $I_z$  on the photoaphere and the area with strong PVEC density could be a result of successive involvement of new magnetic field lines, located higher than previously reconnected ones, into the reconnection process. In other words, the flare process may consist of a large set of reconnection episodes, probably in different locations in the corona above the PIL (e.g. Zimovets et al. 2018). The moving flare ribbons trace magnetic flux associated with magnetic field lines passing through the reconnection region(s). Analysis of high cadence HMI vector magnetograms revealed expansion of the

regions with strong PVEC density associated with the moving flare ribbons seen in the UV images. It confirms the idea that the total PVEC in the flare region has tendency to grow due to successive involvement of new magnetic field lines in the reconnection process in the corona. Good time matching between the flare energy release efficiency (observed as the time derivative of the SXR emission light curve) and electron acceleration (observed as the HXR and microwave light curves) from one side, and the flare ribbon area, total PVEC and average PVEC density through the ribbons during three subsequent sub-flares (see Figure 15) from another side, confirms additionally that the flare energy release is associated with the involvement of new current-carrying magnetic elements and local amplification of PVEC near the PIL. This should be related to the spatio-temporal dynamics of the current sheet(s) above the PIL.

Here it is appropriate to note a certain analogy of the observed phenomena with the processes in the Earth’s magnetosphere during substorms. It is well known that substorms are the result of magnetic reconnection in the near-Earth magnetotail current sheet (see for review, e.g., Baker et al. 1996; Angelopoulos et al. 2008). This phenomenon is associated with plasma heating and acceleration, generation of earthward and tailward plasma flows accompanied by the magnetic field enhancement, so called dipolarization. These plasma flows distort magnetic field lines that leads to generation of magnetic shear and the field-aligned currents as a consequence (see e.g. Kepko et al. 2015, and references therein). Recent observations in the magnetosphere and numerical simulations confirm the close link between plasma outflows from the near-Earth magnetotail reconnection region and generation of the field-aligned currents (e.g. Artemyev et al. 2018). These results indicate “that the dominant role of the near-Earth magnetotail reconnection in the field-aligned current generation is likely responsible for their transient nature”. The situation could be ideologically similar in the flare investigated in the present work. The active region around the PIL already contained significant quasi-steady electric currents before the flare (and

after it), probably generated as a result of long-lasting horizontal movements of the foot of the magnetic loops. The transient amplifications of the vertical currents on the photosphere during the energy release in the sub-flares could be associated with plasma outflows and magnetic field enhancement as the result of magnetic reconnection episodes in the current sheet(s) above the PIL. Further research should show how justified such an analogy is.

There is an alternative mechanism, which could possibly explain the monotonically rising total PVEC during the flare impulsive phase in the region near the PIL. Together with the magnetic reconnection process spreading from the lower to higher loops and involving new magnetic flux connected with the flare ribbons one could suspect something like of inertia of the electric current system due to electrical inductance of the current-carrying magnetic loops. Indeed, let's imagine that magnetic reconnection generates the electromotive force  $\varepsilon$  (e.m.f.) and magnetic loops with plasma attached to the reconnection region in the lower solar atmosphere will be complex load with inductance  $L$  and resistance  $R$ . Then an equation describing temporal evolution of electric current is:

$$RI(t) + \frac{d(LI(t))}{dt} = \varepsilon.$$

In general case  $R$ ,  $L$  and  $\varepsilon$  are functions of time. In the simplest case, for the constant values one has:

$$I(t) = \varepsilon/R(1 - \exp(-Rt/L)).$$

In other words, appearance of a generator will not lead to immediate response in the electric current. In the simplest case, current grows exponentially with the characteristic time  $L/R$ . With a more real description of all terms in the above equation one can estimate the growth rate of the electric current to compare it with observations. It is out of the scope of this work and requires separate research. It is worth noting that the inductance of the flare electric current circuit and simultaneous expansion of magnetic reconnection in the flare region can be a suitable reason to explain the observed dynamics of PVEC. However,

we need detailed theoretical and observational investigation of this phenomenon as it is not clear whether dissipation could suppress electric induction or not.

## 6.5. ACCELERATION OF ELECTRONS

As we know from Paper I, electrons were accelerated up to the kinetic energy  $K_0 \sim 0.1$  MeV in the first sub-flare of the flare studied. A small fraction of electrons could be accelerated to higher energies ( $\sim 1$  MeV), as evidenced by the presence of detectable non-thermal gyrosynchrotron microwave radiation, but could not be registered in the HXR range because of the background. Thus, the lower limit for the maximal kinetic energy of non-thermal electrons is considered here as  $K_0 \sim 0.1$  MeV. From tracing of the flare ribbons we found the magnetic reconnection rate related to the electric field in the current sheet. Firstly, we notice that the reconnection rate estimated for three sub-flares is in qualitative accordance with the observed heating rate (the time derivative of the SXR light curve) and microwave light curves related to the gyrosynchrotron radiation of accelerated electrons. In other words, electron acceleration and heating rate correlates roughly with electric field in the current sheet.

In this subsection we will discuss a possible acceleration process during the first sub-flare when the population of non-thermal electrons was the most energetic among three sub-flares. In the second and third sub-flares, the situation could, in general, repeat the situation in the first sub-flare, but with lower intensity. The maximum value of the electric field in the current sheet was estimated above in order of magnitude as  $E \sim 1/L_{[Mm]} \sim 1$  statvolt/cm (or  $\sim 3 \times 10^2$  V/cm) for  $L = 1$  Mm. This electric field highly exceeds the Dreicer field  $E_D \approx 10^{-11} \ln \Lambda n_e T_e^{-1} \sim 10^{-6}$  statvolt/cm (or  $\sim 10^{-4}$  V/cm), where  $\ln \Lambda \approx 20$  is the Coulomb logarithm,  $n_e \approx 10^{11} \text{ cm}^{-3}$  and  $T_e \approx 40$  MK is the electron plasma density and temperature in the acceleration site, respectively (see Paper I).

Considering the acceleration length scale  $L_{acc} \approx 10$  Mm, corresponding to the length of the accelerated electron capture region obtained in Paper I (i.e. the region where the accelerated electrons were trapped and emitted the gyrosynchrotron radiation detected), one can deduce the maximal accelerated electron energy  $W_1 = eEL_{acc} \approx 300$  GeV, which was actually not observed ( $W_1 \gg K_0$ ). This indicates that, most probably, the electron acceleration length scale was several orders of magnitude less than the electron capture length scale. Considering the results of Litvinenko (1996), one can deduce the maximal energy gained as  $W_2 = eE_{\parallel}\delta B_{\parallel}/B_{\perp}$ . Here the current sheet is assumed to be non-neutralized with the longitudinal  $B_{\parallel}$  and transverse  $B_{\perp}$  magnetic components. For  $\delta \sim 6 \times 10^4 - 6 \times 10^6$  cm (see above) and  $B_{\parallel}/B_{\perp} \sim 10$  (that is reasonable for the flare studied, see Paper I), one can obtain  $W_2 \approx 0.2 - 20$  GeV.

The estimated energies  $W_1$  and  $W_2$  of non-thermal electrons are much higher than the observed ones, i.e.  $W_1 \ll W_2 \ll K_0$ . It means that if the mechanism of the super-Dreicer electric DC field acceleration is valid, than: (1) the inflow plasma velocity should be  $10^3 - 10^5$  times lower (i.e.  $v'_{in} \sim 3.5 - 350$  m/s), or (2) the reconnection current sheet width ( $\delta_{rec}$ ) should be at least  $\sim 10^3$  times smaller than the minimum value of the current sheet width  $\delta_{min} \approx 6 \times 10^4$  cm estimated above from the continuity equation, i.e.  $\delta_{rec} \sim 10 - 100$  cm. The first possibility seems to be unrealistic, as the inflow velocity was estimated from the reconnection rate, which is consistent in order of magnitude with the previous estimations. The second possibility is more likely. Our estimation of  $\delta$  is based on the continuity equation (1), where all parameters ( $n_{in}$ ,  $n_0$ ,  $v_{in}$ ,  $v_A$ ,  $l$ ) can not be measured precisely. Probably, the greatest uncertainty is in estimating the height of the reconnecting current sheet  $l$ . We took an estimate of  $l \sim 1$  Mm from the EUV observation of the bright worm-like structure over the PIL. In fact, the height of the current sheet could be much lower, and the apparent thickness of this EUV structure could be determined by the expansion (outflow) of the heated plasma leaving the reconnection region. It is possible

that the actual height scale of the reconnecting current sheet may be several orders of magnitude lower than our estimation of  $l$ , and then the reconnecting current sheet width could be  $\delta_{rec} \sim 10 - 100$  cm. Here we can also add that this  $\delta_{rec}$  should be considered as a characteristic spatial scale of electron acceleration to the observed energies. This means that the current sheet itself could be much thicker (with  $\delta \sim 6 \times 10^4 - 6 \times 10^6$  cm), but it had filamentation with a characteristic scale  $\delta_{rec}$ , which could impede effective acceleration to higher energies.

Let's estimate the electron acceleration time:  $\Delta t_{acc} = \sqrt{(B_{||}/B_{\perp})(2\delta_{rec}m_e)/(eE_{||})} \sim 10^{-8} - 10^{-7}$  s, where  $m_e$  and  $e$  is the electron mass and charge, respectively (see Aschwanden 2004). The resulting estimate shows that electrons are gaining energy very quickly, much faster than the observed time scales. From this point of view, this acceleration process does not contradict the available observations. Electrons can gain energy quickly, and then they can precipitate to the chromosphere or can be trapped in magnetic loops for quite a long time, emitting HXR and microwave radiations. Each observed burst of HXR and microwave emission with time scale of several seconds (or tens of seconds) could consist of millions of “elementary” bursts (e.g. Kaufmann 1985; Emslie & Henoux 1995), each of which is associated with acceleration in the current filament of scale  $\delta_{rec}$ .

Let's also compare the rate of energy gain due to acceleration by the super-Dreicer field ( $dW_{SD}/dt$ ) and the loss rate due to gyrosynchrotron radiation ( $dW_{gs}/dt$ ):  $dW_{SD}/dt \sim 10^7 E_{||[\text{statvolt/cm}]} \sqrt{1 - (m_e c^2/W)^2}$  MeV/s and  $dW_{gs}/dt \sim -10^{-9} (B_{[G]})^2 (W/m_e c^2)^2$  MeV/s (e.g. Longair 1981). Consequently,  $dW_{SD}/dt > |dW_{gs}/dt|$  for electron energy  $W \lesssim 500$  GeV under the estimated  $E_{||} \approx 1$  statvolt/cm and  $B \approx 1000$  G. This means that for the kinetic energies of accelerated electrons ( $K \lesssim 1$  MeV) observed in the flare studied the energy gain due to acceleration in the super-Dreicer field estimated far surpasses the energy loss due to gyrosynchrotron radiation, and the latter can be neglected. The characteristic time

of energy loss due to gyrosynchrotron radiation (after leaving the acceleration region) is  $\Delta t_{gs} \approx 10^9 \times (m_e c^2) K_0 / [B_{[G]}^2 (K_0 + m_e c^2)] \approx 80 - 330$  s for  $K_0 \sim 0.1 - 1$  MeV and  $B \approx 1000$  G, which is comparable with the duration of the sub-flares observed.

To sum up the above estimations, there is no problem to produce electrons with energies sufficient to generate HXR and microwave emissions by the estimated super-Dreicer electric field. The problem is that such “ideal” accelerator seems to be too efficient and could accelerate electrons to much higher energies than the observed ones. Possibly, an efficiency of a real accelerator may be much different due to presence of electric current filamentation (fragmentation). In particular, it was shown on the base of 3D kinetic simulation that electrons can effectively gain energy by a Fermi-like mechanism due to reflection from contracting field lines during reconnection in a filamenting current sheet with a guide magnetic field (Dahlin et al. 2015). A similar situation, but in a much larger physical volume than the simulated one, could well be realized in the flare studied. Another possibility of plasma heating and electron acceleration is related to collapsing magnetic loops (traps), which could have been formed above the PIL as a result of the TCMR (see discussion above). In this process, the kinetic energy gain by a particle is roughly proportional to the square of the ratio of lengths of stretched and unstretched trap (Somov & Bogachev 2003; Borissov et al. 2016). It is unlikely that this ratio exceeded  $\approx 2 - 3$  in the confined flare studied. Thus, we suppose that this mechanism, although it could serve as a source of some additional plasma heating and electron acceleration, did not play a crucial role.

From Paper I we know that the ratio of nonthermal electrons to thermal super-hot electrons was  $\approx 0.01$ . Large-scale electric field acts equally on all electrons, whereas we see that only a small part of them was accelerated. Runaway electrons can quickly setup a strong charge separation that screens the electric field. This process can be



also accompanied by excitation of waves/turbulence by beams of runaway electrons and subsequent interaction with them, preventing further effective acceleration (e.g. Boris et al. 1970; Holman 1985). On the other hand, it is known that stochastic acceleration, based on wave-particle interaction, is selective to electrons which are in resonance with waves. Thus, only a fraction of electrons from thermal or initially pre-accelerated populations has a chance to be accelerated further. In the above subsection we discussed necessity to introduce filamentation/turbulence to explain tearing instability and the presence of super-hot plasma. Possibly, this turbulence could accelerate electrons in the frame of the stochastic acceleration models. It could explain the ratio of accelerated electrons to thermal particles and less energies than the estimated ones in the frame of the super-Dreicer DC electric field acceleration. Unfortunately, we should emphasize that it is difficult to prove the presence of turbulence in the flare studied on the base of the available observational data. Finally, it should be mentioned that other acceleration mechanisms could be also considered (e.g. Aschwanden 2004; Zharkova et al. 2011, and references therein) that is, however, out of the scope of this work.

## 6.6. SUMMARY AND CONCLUSIONS

This work and Paper I is an attempt to make detailed investigation of the flare energy release in conditions far from those ones assumed in the “standard” two-dimensional model of eruptive solar flares. Our interest to the selected flare (SOL2015-03-15T22:43), composed of three subsequent sub-flares, was due to its initial energy release development very low in the corona ( $H \approx 3$  Mm), possibly even in the chromosphere, in the region with strong vertical PVEC near the the PIL.

The observational results obtained in these two papers provided us with the information to discuss the basic properties of energy release in the vicinity of the PIL for the confined

solar flare. In this work we used high-cadence 135-second HMI vector magnetograms that allowed us to investigate dynamics of the photospheric magnetic field and PVEC on time scale of the impulsive flare phase.

We compared maps of photospheric magnetic field components and PVEC with the flare images in different ranges of electromagnetic spectrum (optical, UV, EUV, SXR and HXR). Locations of the flare emission sources, as well as the retrieved dynamics of the photospheric magnetic field and extrapolated coronal magnetic field are nicely fitted by the TCMR-based flare scenario.

Analysis of 135-second vector magnetograms revealed that total PVEC shows sharp increase during the flare that confirms the observations obtained with 720-second cadence in the previous works. However, we found that the temporal profile of the effective PVEC density (averaged over the flare region around the PIL) has maximum during the first subflare and subsequent gradual decrease. We think that we found manifestations of electric current dissipation connected with the flare energy release process.

From our point of view, the most important result of this paper is the deduced dynamics of the magnetic field and PVEC inside the flare ribbons. High-cadence magnetograms allowed to investigate non-stationary dynamics of the UV ribbons relative to the structure of magnetic field and PVEC in the flare region. For three consecutive sub-flares, we found rough matching of the plasma heating and electron acceleration efficiency with the magnetic reconnection rate, total PVEC and PVEC density in the flare ribbons. We argued that this observation can be qualitatively interpreted within the TCMR scenario.

In conclusion, we would like to emphasize that to extract more useful information about the flare energy release processes around the PIL, where the magnetic reconnection develops in the conditions far from the 2D picture presented in the standard eruptive flare model, one needs in additional systematic study of the events similar to the discussed

ones. Despite on the large data set analyzed in these two works we still need more detailed observations and advanced modeling of plasma heating and particle acceleration within the TCMR scenario in realistic systems of highly sheared magnetic loops with strong magnetic field and electric currents.

We are grateful to the teams of HMI/SDO, AIA/SDO, RHESSI, SOT/Hinode, NoRP and GOES for the available data used. We thank Drs A.V. Artemyev and D.Y. Kolotkov for fruitful discussions. We also appreciate to the anonymous reviewer for a number of useful comments, which helped to improve the paper. This work is supported by the Russian Science Foundation under grant No. 17-72-20134.

## REFERENCES

- Abramenko, V. I., Gopasiuk, S. I., & Ogir', M. B. 1991, *Sol. Phys.*, 134, 287
- Alfvén, H., & Carlqvist, P. 1967, *Sol. Phys.*, 1, 220
- Amari, T., Canou, A., Aly, J.-J., Delyon, F., & Alauzet, F. 2018, *Nature*, 554, 211
- Angelopoulos, V., et al. 2008, *Science*, 321, 931
- Artemyev, A. V., et al. 2018, *Geophys. Res. Lett.*, 45, 5836
- Asai, A., Yokoyama, T., Shimojo, M., Masuda, S., Kurokawa, H., & Shibata, K. 2004, *ApJ*, 611, 557
- Aschwanden, M. J. 2004, *Physics of the Solar Corona. An Introduction* (Praxis Publishing Ltd)
- Aschwanden, M. J., Xu, Y., & Jing, J. 2014, *ApJ*, 797, 50
- Baker, D. N., Pulkkinen, T. I., Angelopoulos, V., Baumjohann, W., & McPherron, R. L. 1996, *J. Geophys. Res.*, 101, 12975
- Bamba, Y., Lee, K.-S., Imada, S., & Kusano, K. 2017, *ApJ*, 840, 116
- Bogachev, S. A., Somov, B. V., Kosugi, T., & Sakao, T. 2005, *ApJ*, 630, 561
- Boris, J. P., Dawson, J. M., Orens, J. H., & Roberts, K. V. 1970, *Physical Review Letters*, 25, 706
- Borissov, A., Neukirch, T., & Threlfall, J. 2016, *Sol. Phys.*, 291, 1385
- Canfield, R. C., et al. 1992, *PASJ*, 44, L111
- Carmichael, H. 1964, *NASA Special Publication*, 50, 451

- Centeno, R., Schou, J., Hayashi, K., Norton, A., Hoeksema, J. T., Liu, Y., Leka, K. D., & Barnes, G. 2014, *Sol. Phys.*, 289, 3531
- Cheng, X., Guo, Y., & Ding, M. 2017, *Science in China Earth Sciences*, 60, 1383
- Cheng, X., Li, Y., Wan, L. F., Ding, M. D., Chen, P. F., Zhang, J., & Liu, J. J. 2018, *ApJ*, 866, 64
- Chifor, C., Tripathi, D., Mason, H. E., & Dennis, B. R. 2007, *A&A*, 472, 967
- Colgate, S. A. 1978, *ApJ*, 221, 1068
- Dahlin, J. T., Drake, J. F., & Swisdak, M. 2015, *Physics of Plasmas*, 22, 100704
- Démoulin, P., Priest, E. R., & Lonie, D. P. 1996, *J. Geophys. Res.*, 101, 7631
- Emslie, A. G., & Henoux, J.-C. 1995, *ApJ*, 446, 371
- Emslie, A. G., et al. 2012, *ApJ*, 759, 71
- Fainshtein, V. G., Egorov, Y. I., Rudenko, G. V., & Anfinogentov, S. A. 2016, *Geomagnetism and Aeronomy*, 56, 1060
- Fleishman, G. D., & Pevtsov, A. A. 2018, in Washington DC American Geophysical Union Geophysical Monograph Series, Vol. 235, *Electric Currents in Geospace and Beyond*, ed. A. Keiling, O. Marghitu, & M. Wheatland, 43–65
- Forbes, T. G., & Lin, J. 2000, *Journal of Atmospheric and Solar-Terrestrial Physics*, 62, 1499
- Gibson, S. E., Fan, Y., Mandrini, C., Fisher, G., & Demoulin, P. 2004, *ApJ*, 617, 600
- Gibson, S. E., Fan, Y., Török, T., & Kliem, B. 2006, *Space Sci. Rev.*, 124, 131
- Grigis, P. C., & Benz, A. O. 2005, *ApJ*, 625, L143

- Guo, J., Emslie, A. G., & Piana, M. 2013, *ApJ*, 766, 28
- Hinterreiter, J., Veronig, A. M., Thalmann, J. K., Tschernitz, J., & Pötzi, W. 2018, *Sol. Phys.*, 293, 38
- Hirayama, T. 1974, *Sol. Phys.*, 34, 323
- Hoeksema, J. T., et al. 2014, *Sol. Phys.*, 289, 3483
- Holman, G. D. 1985, *ApJ*, 293, 584
- Hood, A. W., & Priest, E. R. 1979, *Sol. Phys.*, 64, 303
- Hurford, G. J., et al. 2002, *Sol. Phys.*, 210, 61
- Isobe, H., Takasaki, H., & Shibata, K. 2005, *ApJ*, 632, 1184
- Isobe, H., Yokoyama, T., Shimojo, M., Morimoto, T., Kozu, H., Eto, S., Narukage, N., & Shibata, K. 2002, *ApJ*, 566, 528
- Janvier, M. 2017, *Journal of Plasma Physics*, 83, 535830101
- Janvier, M., Aulanier, G., Bommier, V., Schmieder, B., Démoulin, P., & Pariat, E. 2014, *ApJ*, 788, 60
- Janvier, M., et al. 2016, *A&A*, 591, A141
- Kaufmann, P. 1985, *Sol. Phys.*, 102, 97
- Kepko, L., et al. 2015, *Space Sci. Rev.*, 190, 1
- Kleint, L., Wheatland, M. S., Mastrano, A., & McCauley, P. I. 2018, *ApJ*, 865, 146
- Kliem, B. 1994, *ApJS*, 90, 719
- Kliem, B., & Török, T. 2006, *Physical Review Letters*, 96, 255002

- Kopp, R. A., & Pneuman, G. W. 1976, *Sol. Phys.*, 50, 85
- Kosovichev, A. G., & Zharkova, V. V. 2001, *ApJ*, 550, L105
- Kosugi, T., et al. 2007, *Sol. Phys.*, 243, 3
- Krucker, S., Hurford, G. J., & Lin, R. P. 2003, *ApJ*, 595, L103
- Kuznetsov, S. A., Zimovets, I. V., Morgachev, A. S., & Struminsky, A. B. 2016, *Sol. Phys.*, 291, 3385
- Leka, K. D., Canfield, R. C., McClymont, A. N., de La Beaujardiere, J.-F., Fan, Y., & Tang, F. 1993, *ApJ*, 411, 370
- Li, J., Metcalf, T. R., Canfield, R. C., Wülser, J.-P., & Kosugi, T. 1997, *ApJ*, 482, 490
- Lin, J., Ko, Y.-K., Sui, L., Raymond, J. C., Stenborg, G. A., Jiang, Y., Zhao, S., & Mancuso, S. 2005, *ApJ*, 622, 1251
- Lin, R. P., et al. 2002, *Sol. Phys.*, 210, 3
- Litvinenko, Y. E. 1996, *ApJ*, 462, 997
- Longair, M. S. 1981, *High energy astrophysics*
- Melrose, D. B. 2017, *Journal of Geophysical Research (Space Physics)*, 122, 7963
- Miklenic, C. H., Veronig, A. M., Vršnak, B., & Hanslmeier, A. 2007, *A&A*, 461, 697
- Moore, R. L., & Roumeliotis, G. 1992, in *Lecture Notes in Physics*, Berlin Springer Verlag, Vol. 399, IAU Colloq. 133: Eruptive Solar Flares, ed. Z. Svestka, B. V. Jackson, & M. E. Machado, 69
- Moore, R. L., Sterling, A. C., Hudson, H. S., & Lemen, J. R. 2001, *ApJ*, 552, 833

- Moreton, G. E., & Severny, A. B. 1968, *Sol. Phys.*, 3, 282
- Musset, S., Vilmer, N., & Bommier, V. 2015, *A&A*, 580, A106
- Narukage, N., & Shibata, K. 2006, *ApJ*, 637, 1122
- Neupert, W. M. 1968, *ApJ*, 153, L59
- Nishizuka, N., Karlický, M., Janvier, M., & Bárta, M. 2015, *ApJ*, 799, 126
- Nita, G. M., Fleishman, G. D., Kuznetsov, A. A., Kontar, E. P., & Gary, D. E. 2015, *ApJ*, 799, 236
- Pesnell, W. D., Thompson, B. J., & Chamberlin, P. C. 2012, *Sol. Phys.*, 275, 3
- Petrie, G. J. D. 2013, *Sol. Phys.*, 287, 415
- Priest, E. 2014, *Magnetohydrodynamics of the Sun*
- Priest, E. R., & Forbes, T. G. 2002, *A&A Rev.*, 10, 313
- Priest, E. R., & Longcope, D. W. 2017, *Sol. Phys.*, 292, 25
- Qiu, J. 2009, *ApJ*, 692, 1110
- Qiu, J., Lee, J., Gary, D. E., & Wang, H. 2002, *ApJ*, 565, 1335
- Qiu, J., Liu, W., Hill, N., & Kazachenko, M. 2010, *ApJ*, 725, 319
- Qiu, J., Longcope, D. W., Cassak, P. A., & Priest, E. R. 2017, *ApJ*, 838, 17
- Romanov, V. A., & Tsap, T. T. 1990, *Soviet Ast.*, 34, 656
- Rudenko, G. V., & Myshyakov, I. I. 2009, *Sol. Phys.*, 257, 287
- Rust, D. M. 1972, *Sol. Phys.*, 25, 141



- Sadykov, V. M., & Kosovichev, A. G. 2017, *ApJ*, 849, 148
- Scherrer, P. H., et al. 2012, *Sol. Phys.*, 275, 207
- Schmieder, B., & Aulanier, G. 2018, in Washington DC American Geophysical Union Geophysical Monograph Series, Vol. 235, *Electric Currents in Geospace and Beyond*, ed. A. Keiling, O. Marghitu, & M. Wheatland, 391–406
- Schrijver, C. J. 2009, *Advances in Space Research*, 43, 739
- . 2016, *ApJ*, 820, 103
- Severnyi, A. B. 1958, *Soviet Ast.*, 2, 310
- Sharykin, I. N., & Kosovichev, A. G. 2015, *ApJ*, 808, 72
- Sharykin, I. N., Kosovichev, A. G., & Zimovets, I. V. 2015, *ApJ*, 807, 102
- Sharykin, I. N., Sadykov, V. M., Kosovichev, A. G., Vargas-Dominguez, S., & Zimovets, I. V. 2017, *ApJ*, 840, 84
- Sharykin, I. N., Zimovets, I. V., Myshyakov, I. I., & Meshalkina, N. S. 2018, *ApJ*, 864, 156
- Shibata, K., & Magara, T. 2011, *Living Reviews in Solar Physics*, 8, 6
- Shibata, K., & Tanuma, S. 2001, *Earth, Planets, and Space*, 53, 473
- Somov, B. V., & Bogachev, S. A. 2003, *Astronomy Letters*, 29, 621
- Sturrock, P. A. 1966, *Nature*, 211, 695
- Su, Y., Veronig, A. M., Holman, G. D., Dennis, B. R., Wang, T., Temmer, M., & Gan, W. 2013, *Nature Physics*, 9, 489
- Sudol, J. J., & Harvey, J. W. 2005, *ApJ*, 635, 647

- Sun, X., Hoeksema, J. T., Liu, Y., Kazachenko, M., & Chen, R. 2017, *ApJ*, 839, 67
- Sun, X., Hoeksema, J. T., Liu, Y., Wiegelmann, T., Hayashi, K., Chen, Q., & Thalmann, J. 2012, *ApJ*, 748, 77
- Takasao, S., Asai, A., Isobe, H., & Shibata, K. 2012, *ApJ*, 745, L6
- Thalmann, J. K., Su, Y., Temmer, M., & Veronig, A. M. 2015, *ApJ*, 801, L23
- Threlfall, J., Hood, A. W., & Priest, E. R. 2018, *Sol. Phys.*, 293, 98
- Török, T., & Kliem, B. 2005, *ApJ*, 630, L97
- Tsuneta, S., et al. 2008, *Sol. Phys.*, 249, 167
- van Driel-Gesztelyi, L., Hofmann, A., Demoulin, P., Schmieder, B., & Csepura, G. 1994, *Sol. Phys.*, 149, 309
- Vorpahl, J. A. 1976, *ApJ*, 205, 868
- Wang, H., Cao, W., Liu, C., Xu, Y., Liu, R., Zeng, Z., Chae, J., & Ji, H. 2015, *Nat. Commun.*, 6
- Wang, H., Ewell, Jr., M. W., Zirin, H., & Ai, G. 1994, *ApJ*, 424, 436
- Wang, H., et al. 2017, *Nature Astronomy*, 1, 0085
- Wang, R., Liu, Y. D., Hoeksema, J. T., Zimovets, I. V., & Liu, Y. 2018, *ApJ*, 869, 90
- Wheatland, M. S., Sturrock, P. A., & Roumeliotis, G. 2000, *ApJ*, 540, 1150
- Yang, Y.-H., Cheng, C. Z., Krucker, S., & Hsieh, M.-S. 2011, *ApJ*, 732, 15
- Yang, Y.-H., Cheng, C. Z., Krucker, S., Lin, R. P., & Ip, W. H. 2009, *ApJ*, 693, 132
- Yokoyama, T., Akita, K., Morimoto, T., Inoue, K., & Newmark, J. 2001, *ApJ*, 546, L69

- Zaitsev, V. V., Kronshtadtov, P. V., & Stepanov, A. V. 2016, *Geomagnetism and Aeronomy*, 56, 903
- Zaitsev, V. V., & Stepanov, A. V. 2015, *Sol. Phys.*, 290, 3559
- Zharkova, V. V., et al. 2011, *Space Sci. Rev.*, 159, 357
- Zimovets, I. V., Gros, M., & Struminsky, A. B. 2009, *Advances in Space Research*, 43, 680
- Zimovets, I. V., & Struminsky, A. B. 2009, *Sol. Phys.*, 258, 69
- Zimovets, I. V., Wang, R., Liu, Y. D., Wang, C., Kuznetsov, S. A., Sharykin, I. N., Struminsky, A. B., & Nakariakov, V. M. 2018, *Journal of Atmospheric and Solar-Terrestrial Physics*, 174, 17

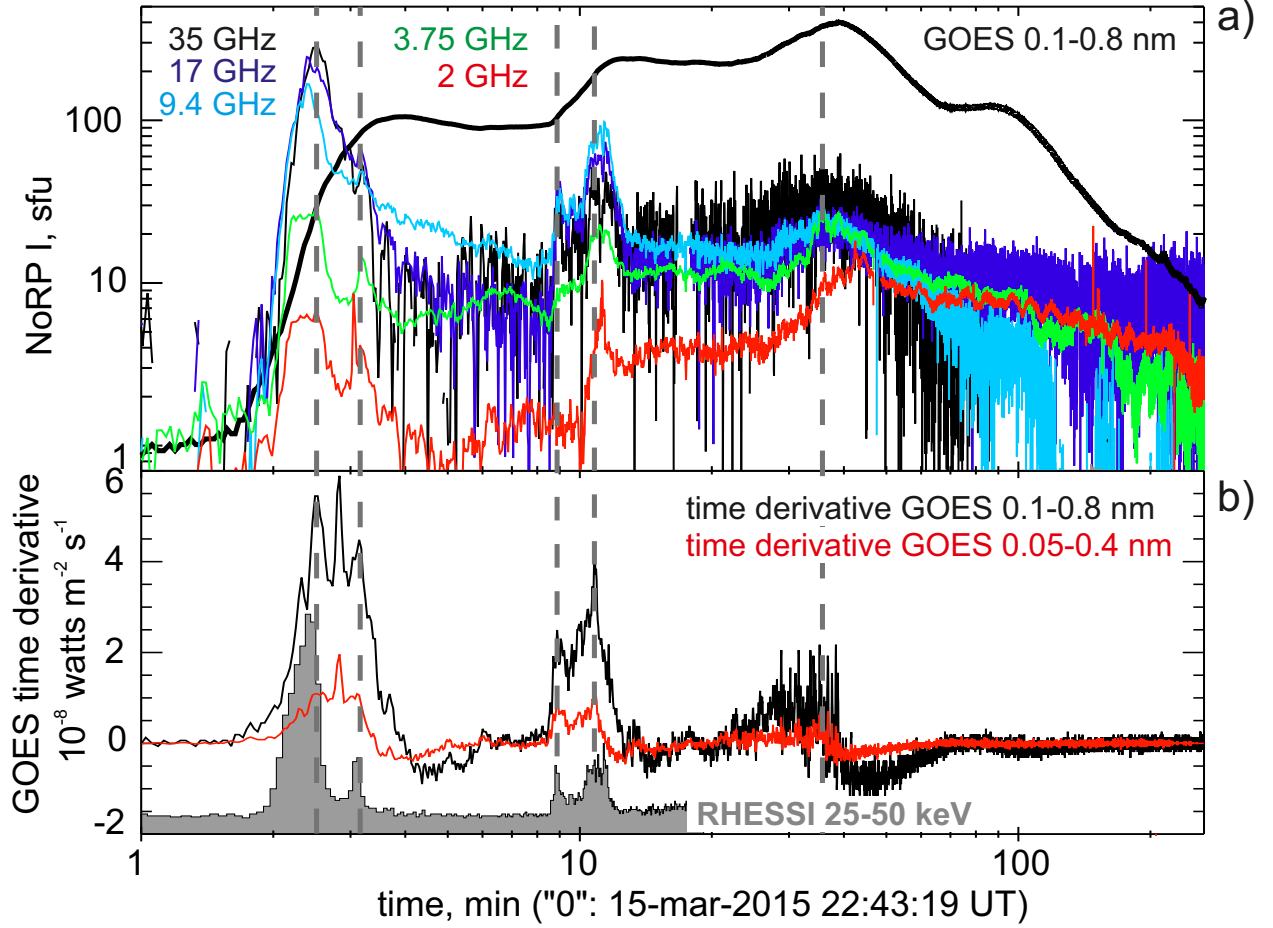


Fig. 1.— Time profiles of the M1.2 solar flare on 15 March 2015, on a logarithmic time scale. a) GOES 1-8 Å lightcurve (thick black line; arbitrary units) and NoRP Stokes  $I$  time profiles at 2, 3.75, 9.4, 17, and 35 GHz (colors are indicated in the plot). b) Time derivatives of the GOES lightcurves in both bands (black and red) and RHESSI lightcurve in the energy band of 25-50 keV in arbitrary units (grey histogram). Vertical dashed lines correspond to time moments of some local maxima of GOES lightcurve time derivatives. They correspond to the microwave local maxima and they are plotted for more convenient comparison between the NoRP time profiles and time derivatives of the GOES lightcurves.

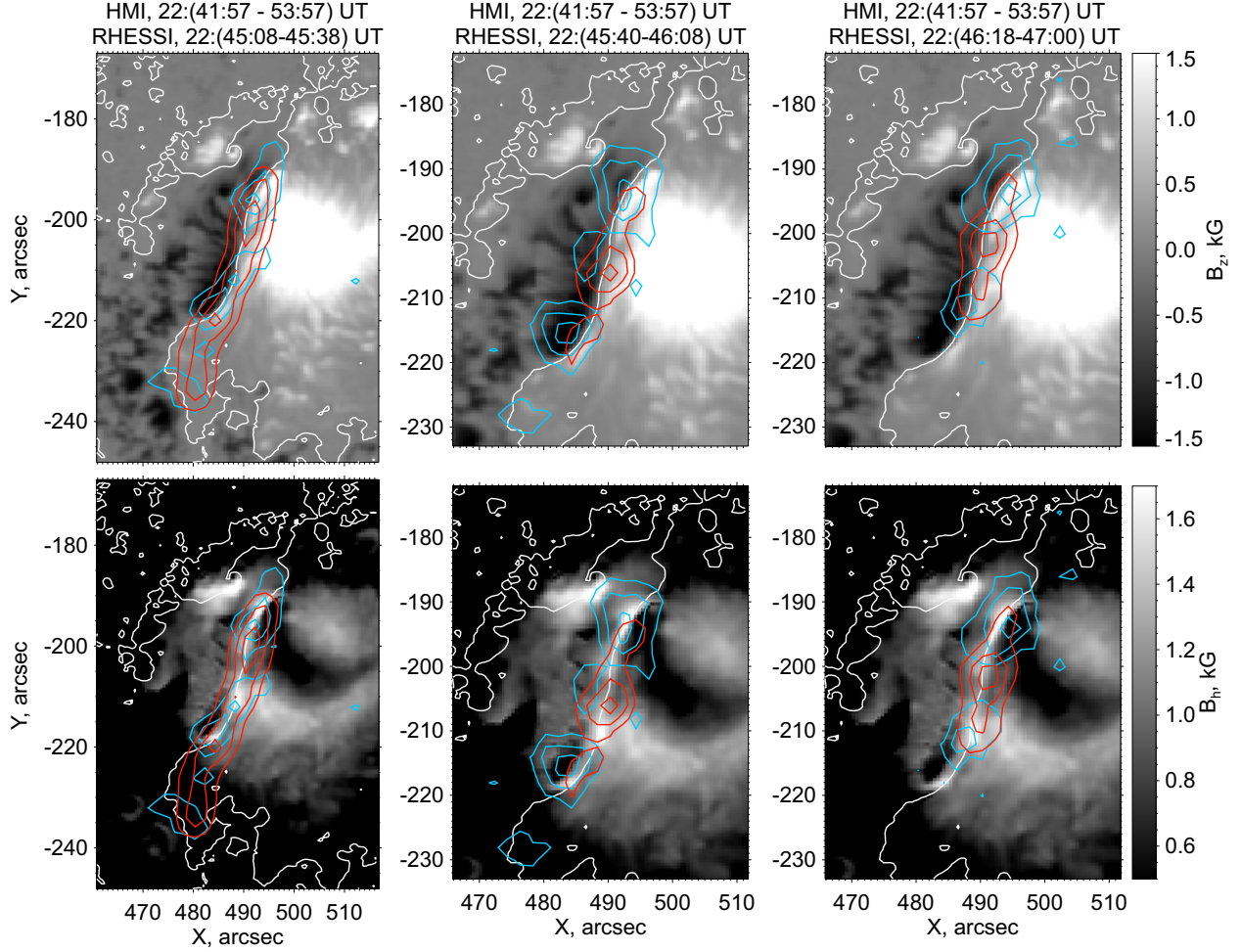


Fig. 2.— Location of the X-ray sources detected by RHESSI in the 6–12 (red) and 25–50 keV (light blue) energy bands in three time intervals (from left to right) during the first subflare of the 15 March 2015 flare studied. Contours correspond to 50, 70, and 90 % levels of the maximal X-ray intensity. The corresponding time intervals are indicated above the top panels. Top and bottom panels present HMI vector magnetograms showing distributions of the vertical and horizontal magnetic field components on the photosphere, respectively. The photospheric PIL is shown by the white curves. Note that the field-of-view size is centered relative to the RHESSI contours and slightly differs for the left and middle and right panels.

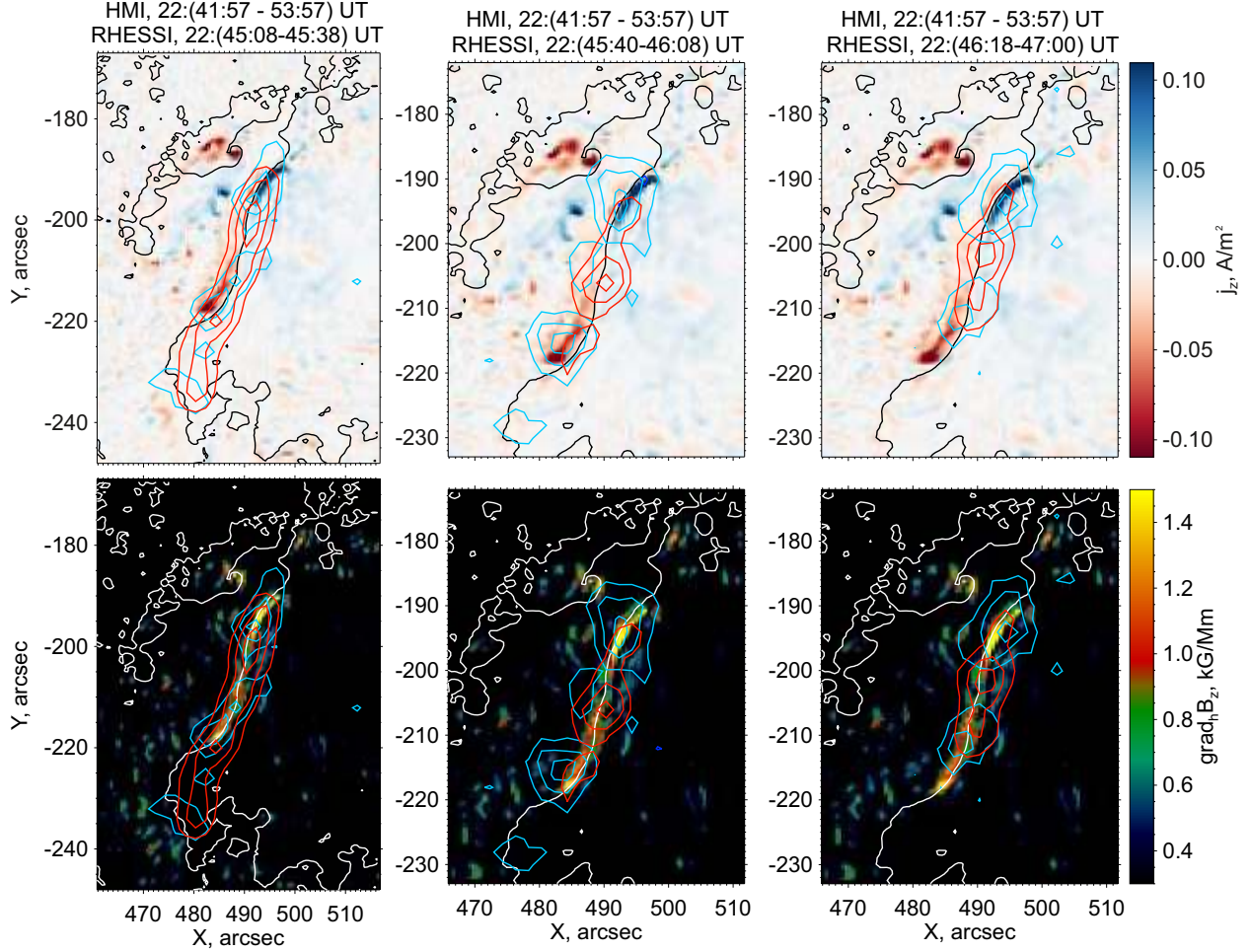


Fig. 3.— Comparison between the RHESSI X-ray contour maps in the energy bands of 6-12 (red) and 25-50 keV (light blue) for three different time intervals (indicated above the top panels) and the maps showing distribution of the vertical electric currents (top panels) and horizontal gradient of vertical magnetic field component (bottom panels) deduced from the 720-second HMI vector magnetogram. The photospheric PIL is shown by the black (top) and white (bottom) curves. RHESSI X-ray contours correspond to 50, 70, and 90 % levels of the maximal X-ray intensity. Note that the field-of-view size is centered relative to the RHESSI contours and differs for the left and middle and right panels.

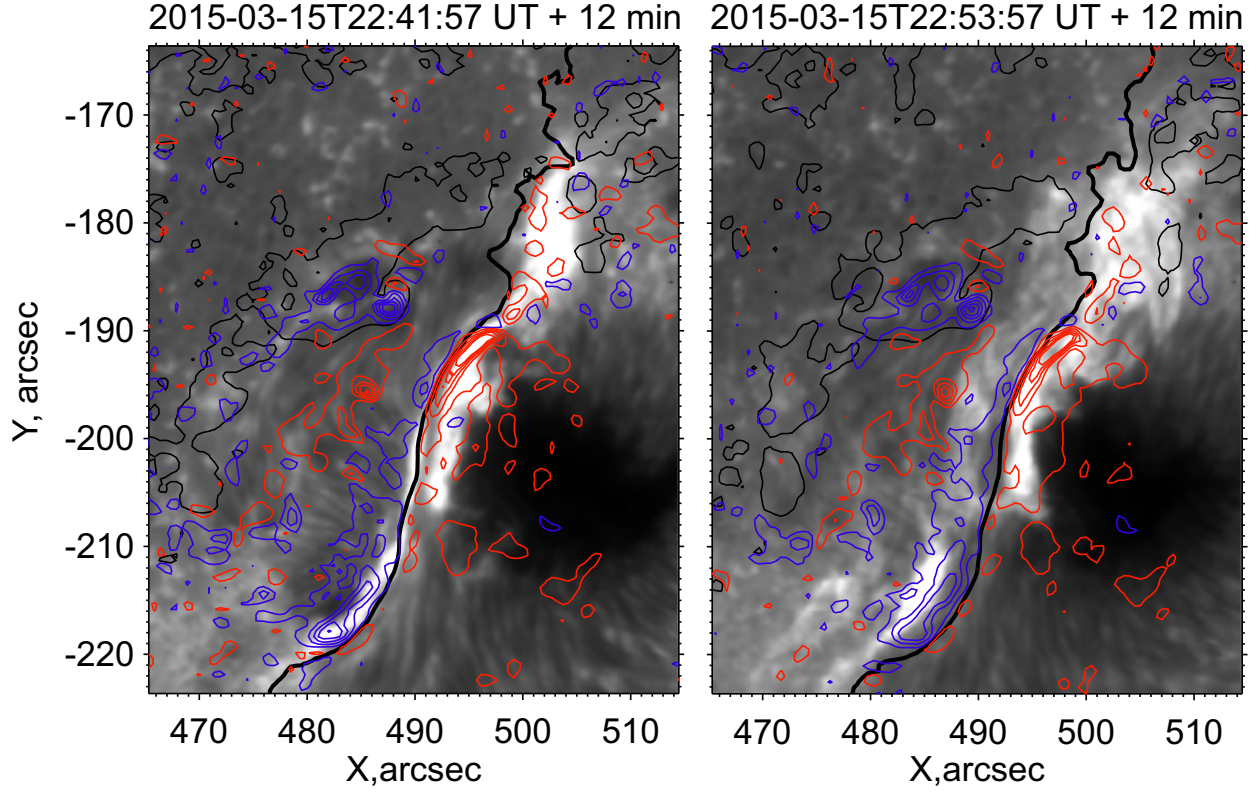


Fig. 4.— Comparison between Ca II SOT/Hinode cumulative image (background) and contour map of the PVEC and the PIL (black curve) deduced from the HMI vector magnetograms. The left and right panels show two subsequent time intervals. The red and blue contours ( $3\sigma(j_z)$  and  $5\sigma(j_z)$ ) correspond to the negative and positive PVEC, respectively. The SOT cumulative image is a result of summing Ca II images taken in time range of 12 min corresponding to the HMI vector magnetograms.



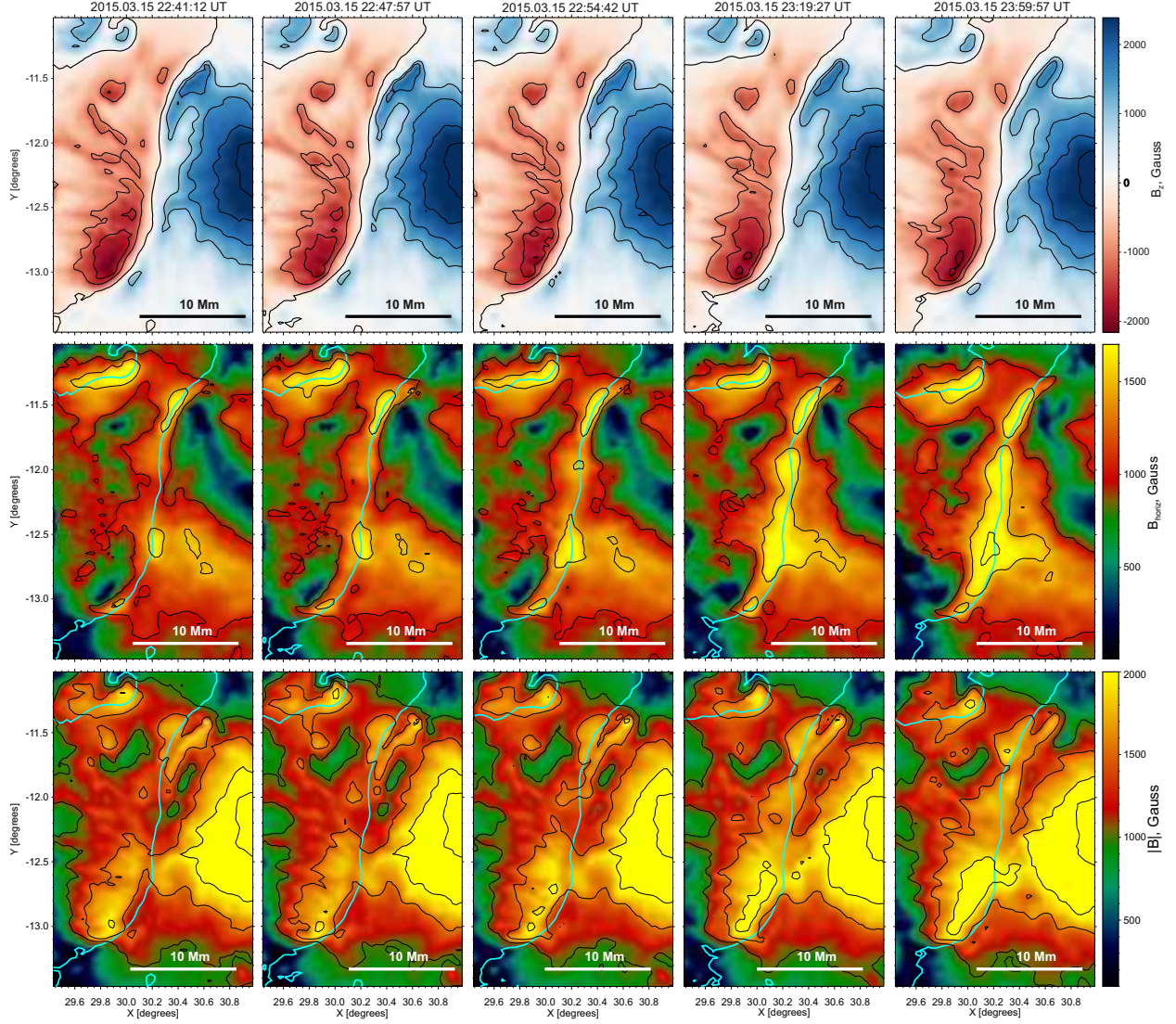


Fig. 5.— Time sequence (time is growing from left to right) of magnetic field component maps, deduced from HMI 135-second vector magnetograms and reprojected onto the heliographic grid. The time is indicated above the top panels. The top, middle and bottom panels correspond to the vertical, horizontal magnetic component and absolute value of the magnetic field, respectively. The photospheric PIL is shown by the black (top) and cyan (middle, bottom) curves.



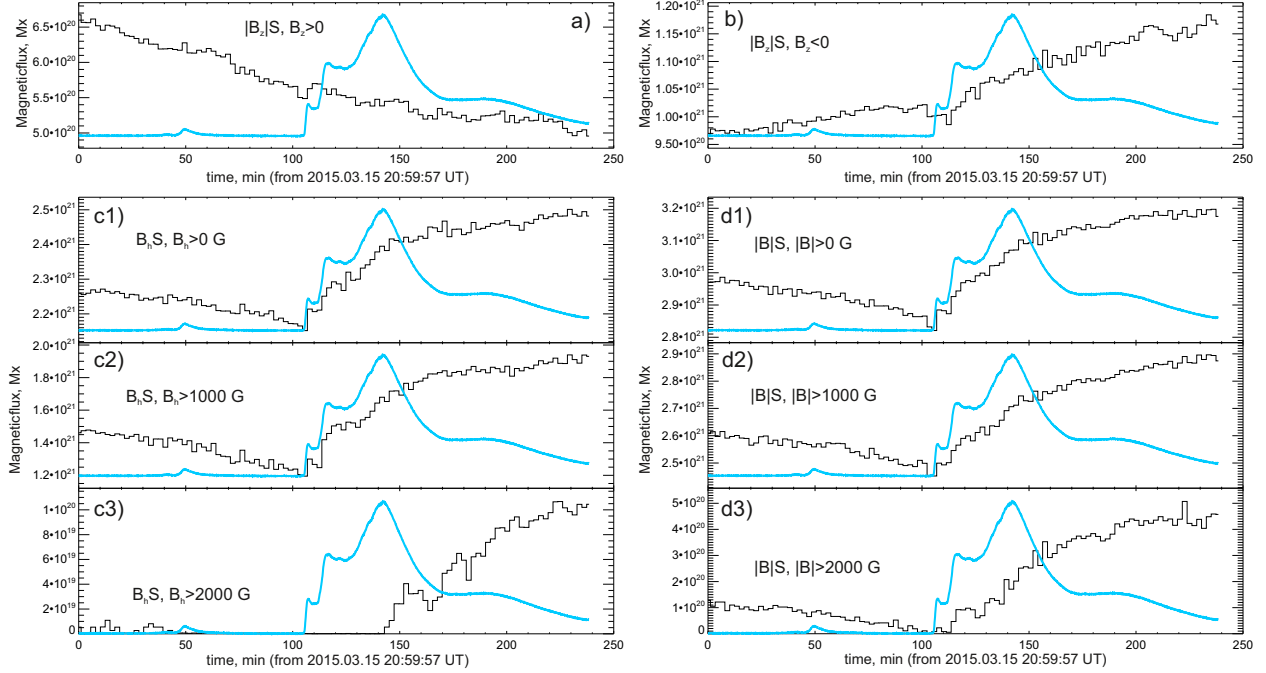


Fig. 6.— Temporal profiles of magnetic fluxes in the PIL region around the strongest PVEC. To compare with real magnetic flux  $B_z S$ , we introduce nominal magnetic flux for the horizontal component and absolute value of the magnetic field. It means that we show sum of magnetic field pixel values multiplied by total area. The analyzed region is shown by the black contour in Fig. 8(a). Panels show the next information: a) magnetic flux for vertical magnetic field component with positive sign. b) Magnetic flux for vertical magnetic field component with negative sign. c1–c2) Magnetic fluxes for horizontal magnetic field component summing pixels with  $B_h > 0$ , 1000, and 2000 G., respectively d1–d2) Magnetic fluxes for magnetic field absolute value summing pixels with  $|B| > 0$ , 1000, and 2000 G, respectively. The blue curve in panels (a–d) is the GOES X-ray lightcurve (1–8 Å) in arbitrary units.

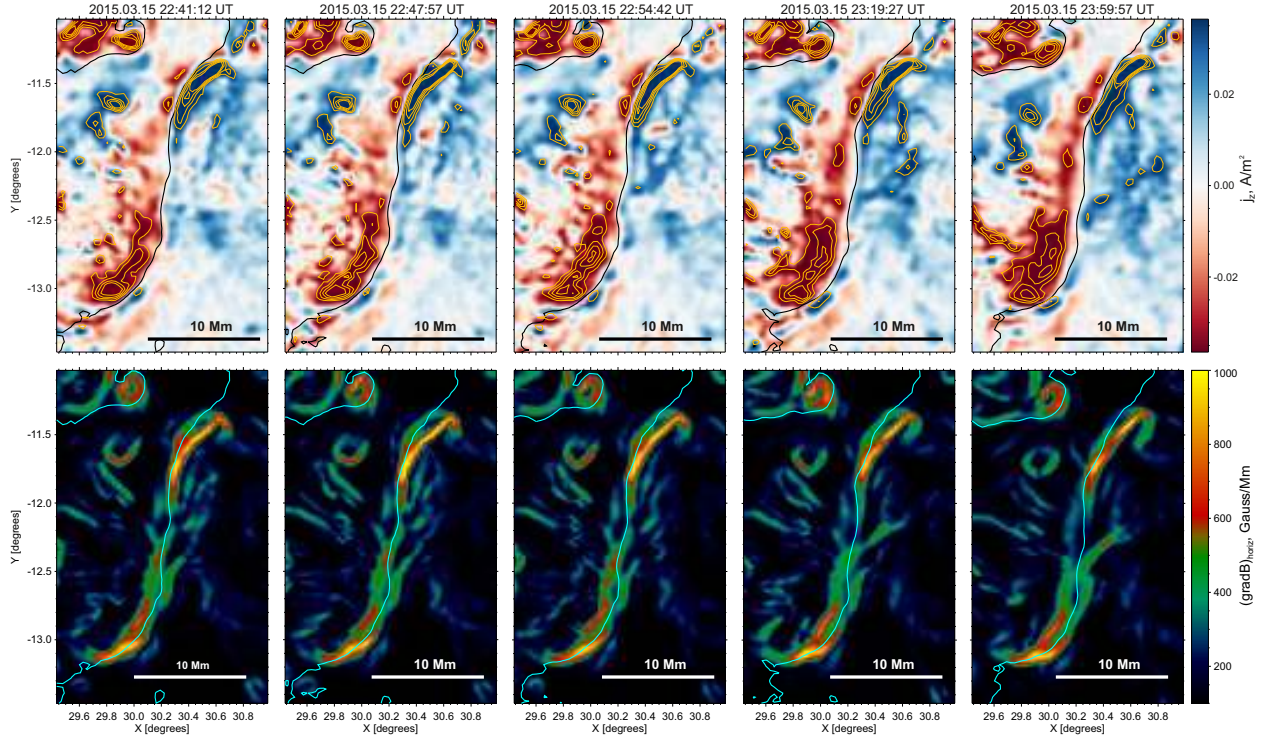


Fig. 7.— Temporal sequence (corresponding time is indicated above the top pannels) of maps showing spatial distributions of PVEC (top panels) and horizontal gradient of the vertical magnetic field component (bottom panels). These maps are deduced from the HMI 135-sec vector magnetograms and reprojected onto the heliographic grid. The photospheric PIL is shown by the black (top) and cyan (bottom) curves. Orange contours mark PVEC density levels of 39, 62, 85 and 115  $\text{mA/m}^2$  for both  $j_z$  signs.

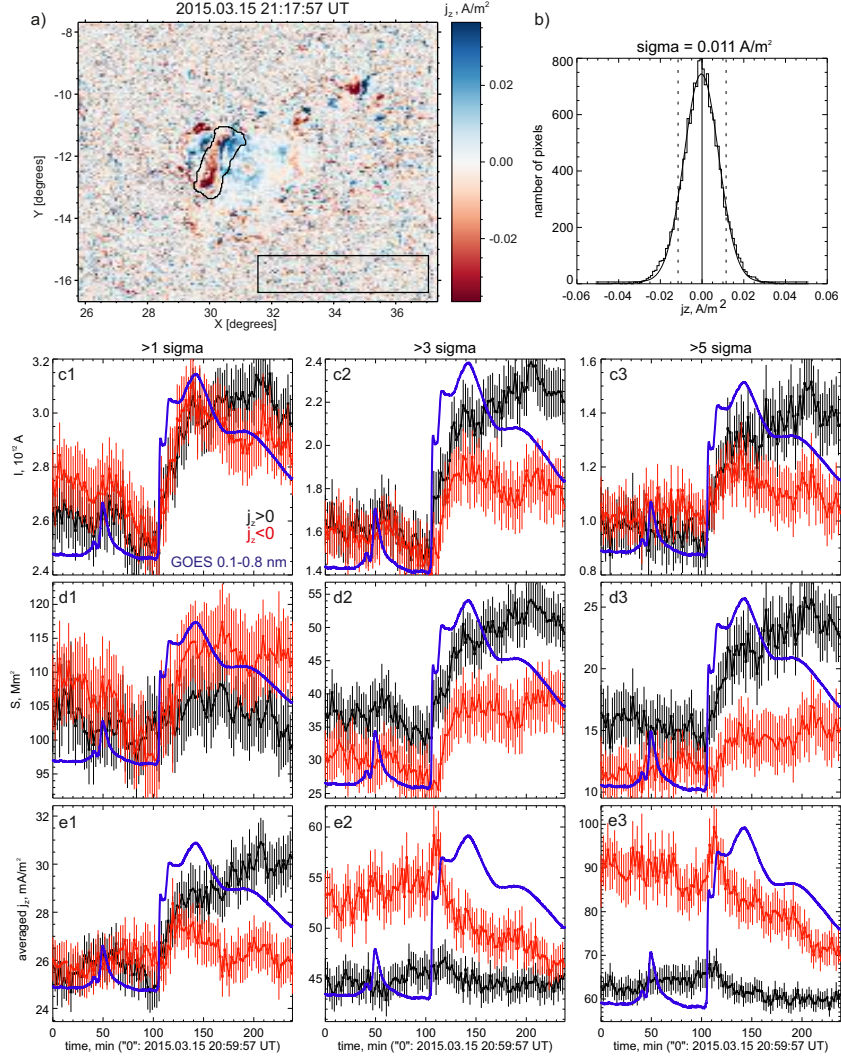


Fig. 8.— Temporal dynamics of the total PVEC  $I_z$  in the flare region (marked by the thick black contour in panel (a)) is shown in the panels (c1)–(c3). Temporal dynamics of area of the regions with the enhanced PVEC is shown in the panels (d1)–(d3). The panels (e1)–(e3) present temporal profiles of the estimated effective PVEC density (ratio of the total PVEC to the area). The measurement errors are shown by the vertical bars. Three panels (from left to right) in each row (c–e) show cases considering the PVEC above the threshold values  $1\sigma(j_z)$ ,  $3\sigma(j_z)$  and  $5\sigma(j_z)$ , respectively. The thin black rectangle in the right-bottom corner of the panel (a) corresponds to the non-flaring (background) region where we calculate the PVEC distribution to determine the noise level  $\sigma(j_z)$ . This distribution is shown in the panel (b) by the histogram, where the solid line is a Gaussian fit. The blue curve in panels (c–e) is the GOES X-ray lightcurve (1–8 Å) in arbitrary units.

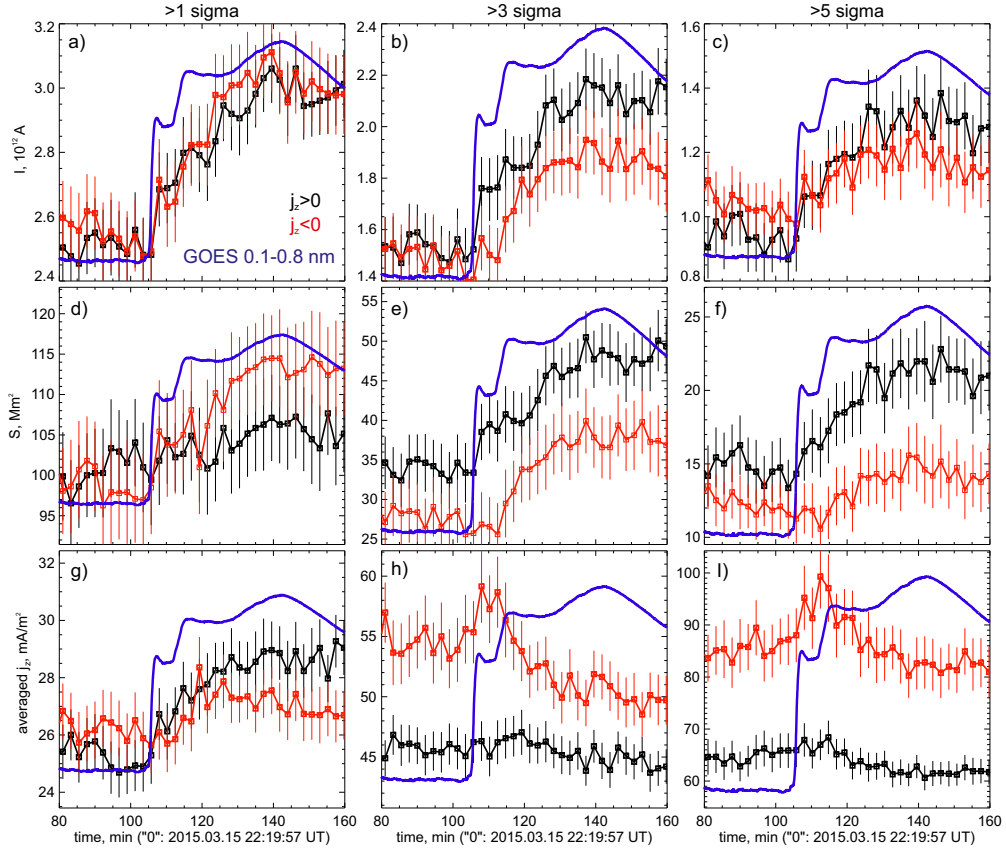


Fig. 9.— This figure is similar to Fig.8(c–e) and has the same content, but shows the corresponding time profiles for the more narrow time range including three subflares studied.

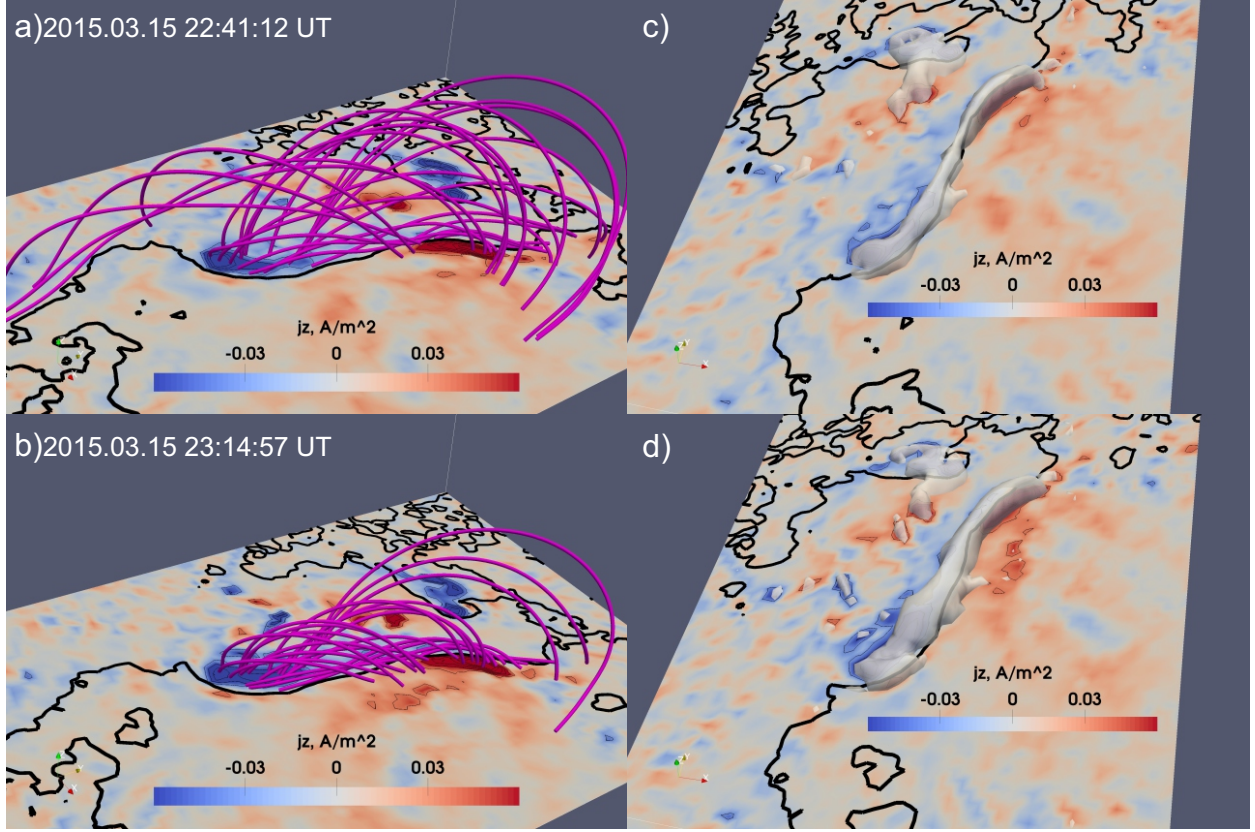


Fig. 10.— Magnetic field lines in the PIL region calculated from the NLFFF magnetic field extrapolations using the HMI 135-sec vector magnetograms as the boundary condition for two different times just before the flare impulsive phase (a) and during main flare X-ray emission peak (b). The regions of strong electric currents flowing along the magnetic field lines for the same times are shown by the white semi-transparent surfaces with the constant level of electric current density of 55 mA/m<sup>2</sup> in (c) and (d), respectively. The base maps show the distributions of vertical electric current density on the photosphere by blue-red (negative-positive) color palette. The thick black curves mark the photospheric PIL.



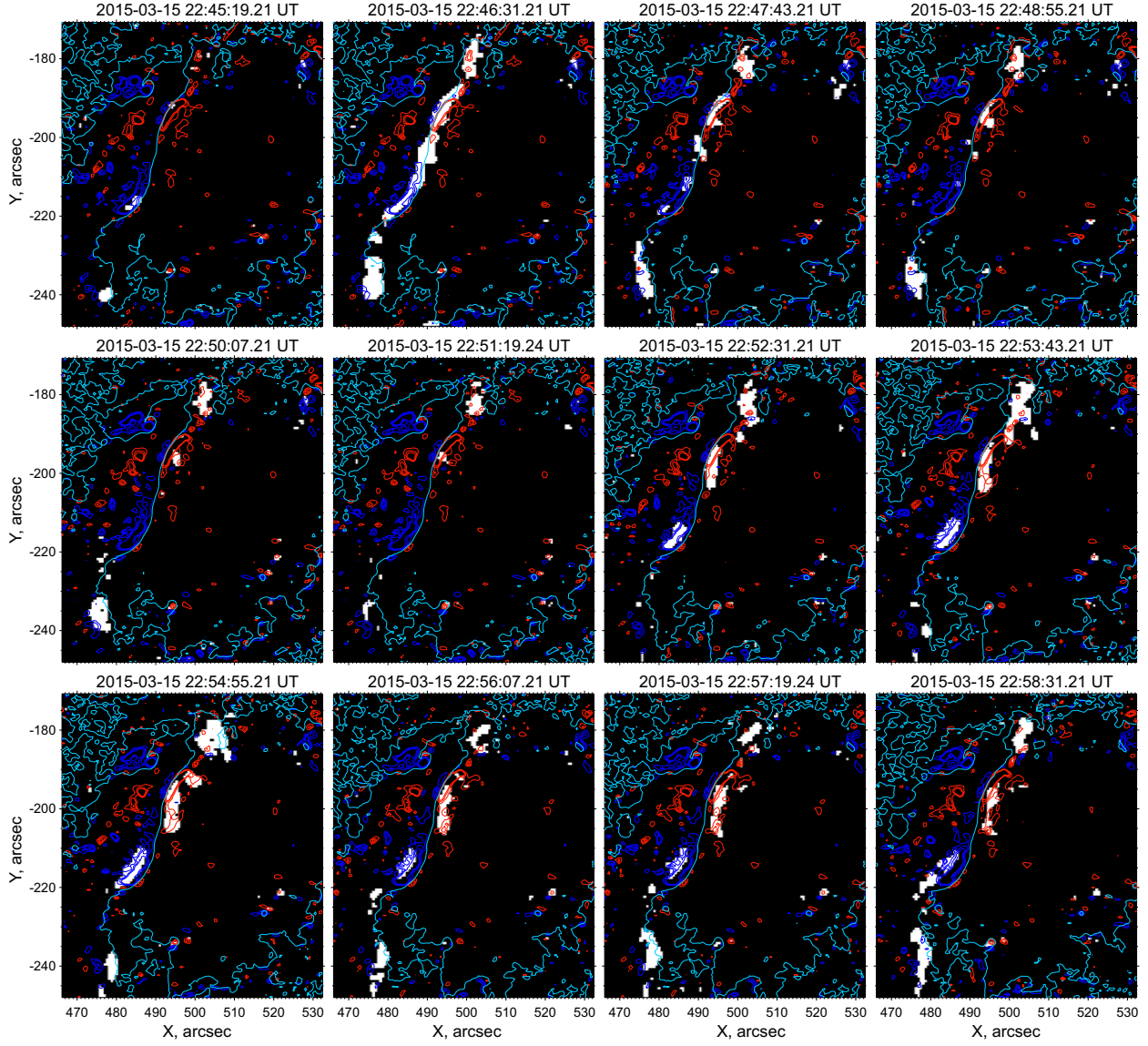


Fig. 11.— Temporal sequence of binary maps (black-white background images) showing the flare ribbon positions deduced from the AIA/SDO UV 1700 Å images. Corresponding times are shown above the panels. Pixels in these maps have only two values: 0 or 1. Value 1 means that this pixel belongs to the flare ribbon. The ribbons were extracted by thresholding images with the threshold value of 3800 DNs. The red and blue contours (23, 39 and 54  $\text{mA/m}^2$ ) correspond to the negative and positive PVEC, respectively. The photospheric PIL is marked by the cyan curves.

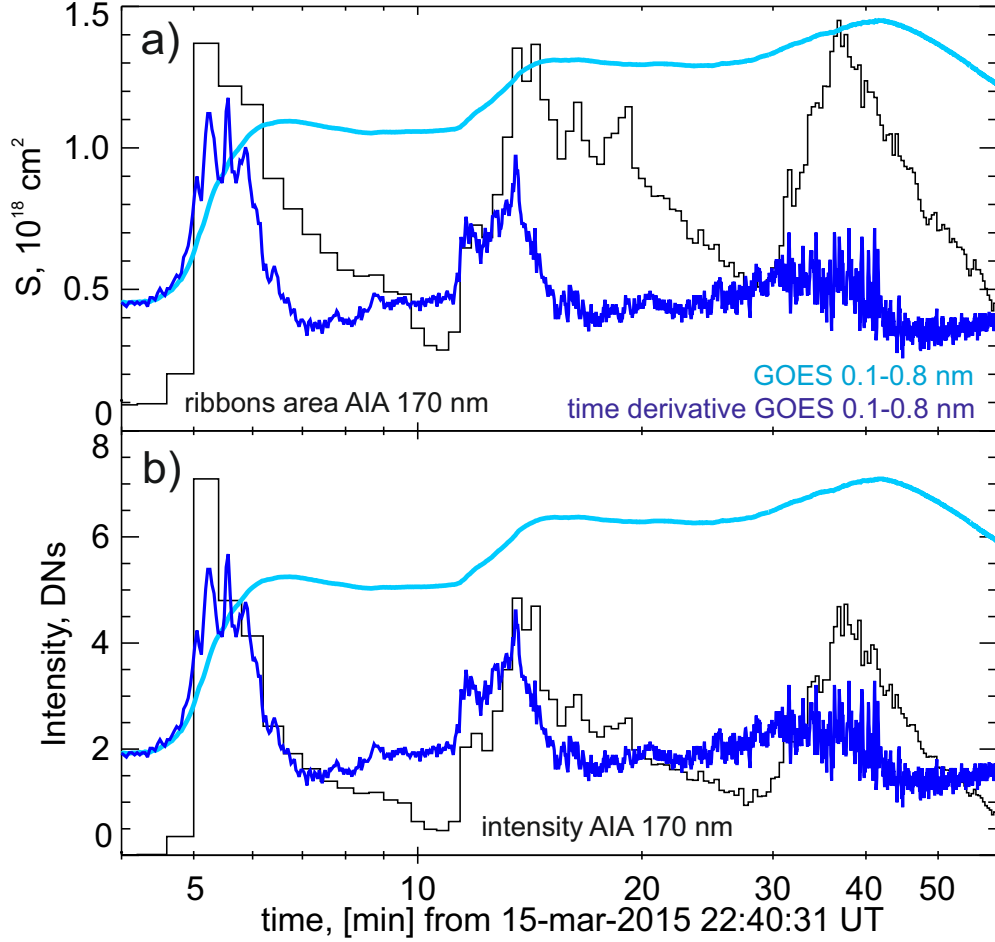


Fig. 12.— Temporal dynamics of the flare ribbon area (black histogram) deduced from the AIA UV 1700 Å images (a). The area is calculated as a sum of pixels with the intensity values higher than the threshold of 3800 DN's (the background images in Fig. 11). The temporal dynamics of the total UV intensity of the flare ribbons is shown in panel (b) by the black histogram. The cyan and blue lines mark the GOES 1-8 Å lightcurve and its time derivative, respectively. Note that time is on a logarithmic scale on the horizontal axis.

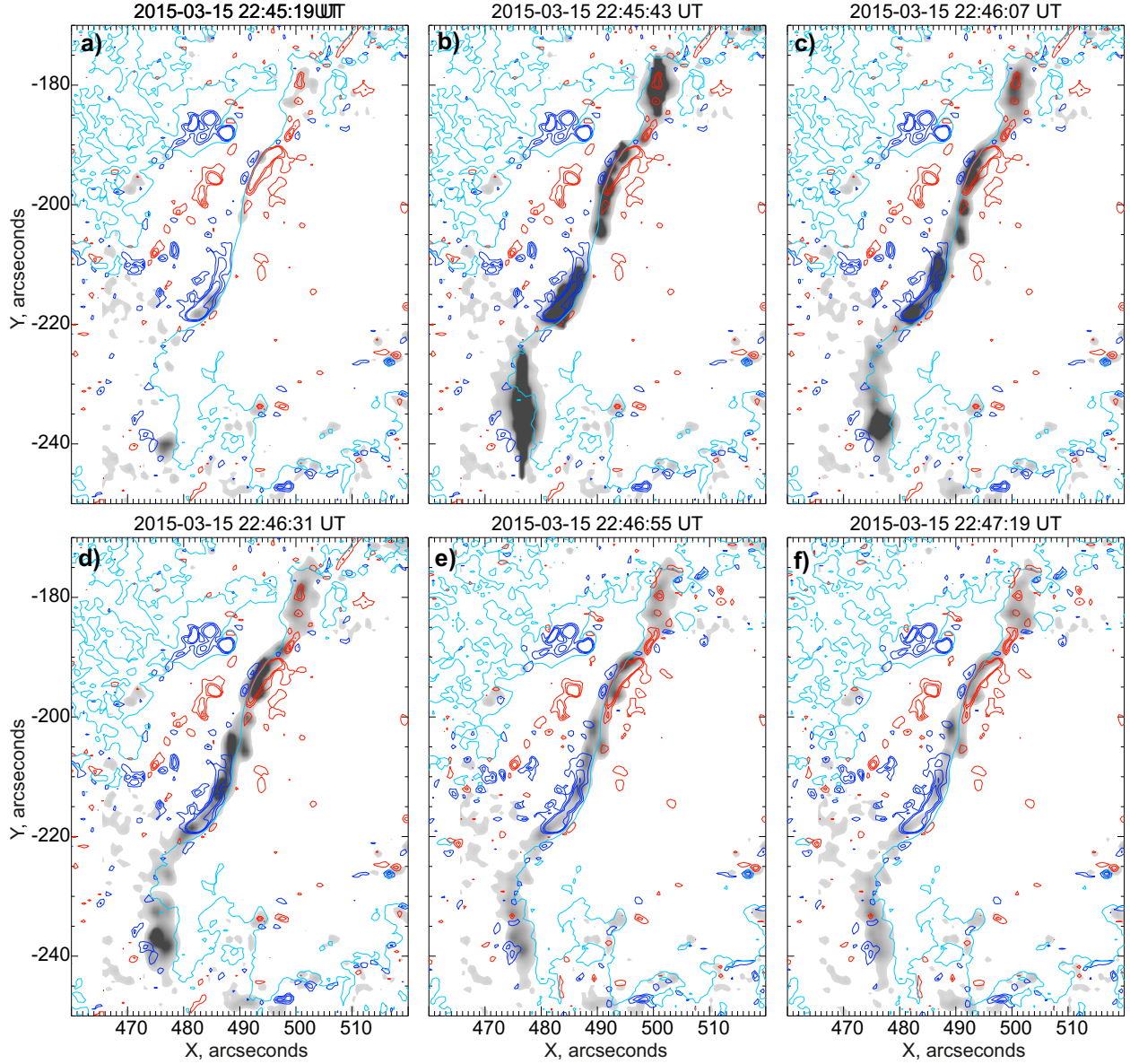


Fig. 13.— Temporal sequence of AIA 1700 Å images (white-black background maps) showing the flare ribbon positions during the first subflare of the 15 March 2015 flare studied. The corresponding time is shown above the panels. The red and blue contours (23, 39 and 54  $\text{mA}/\text{m}^2$ ) correspond to the negative and positive PVEC, respectively. The photospheric PIL is marked by the cyan curves.



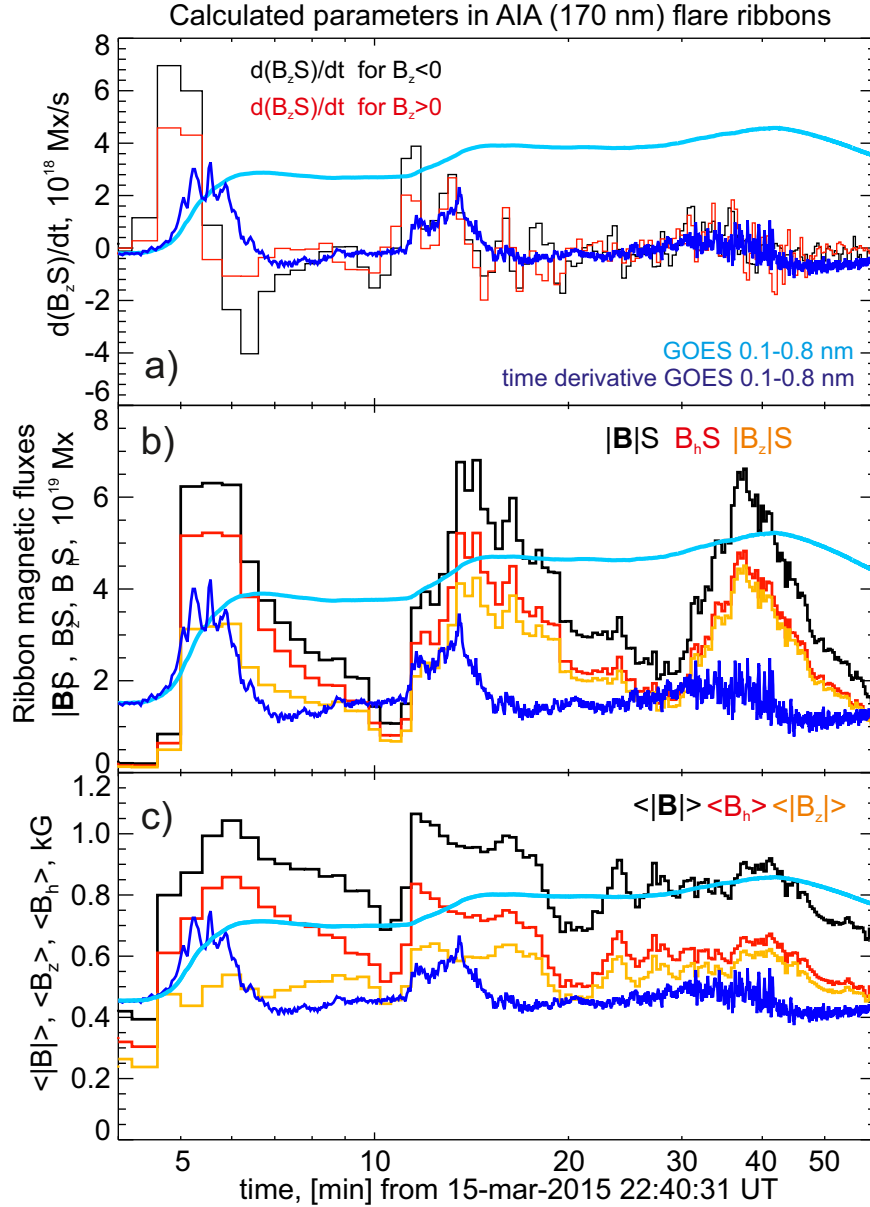


Fig. 14.— (a) Time derivatives of the magnetic (vertical) flux inside the flare ribbons deduced by the thresholding AIA UV 1700 Å images (Fig. 11). The negative and positive fluxes are marked by the black and red colors, respectively. (b) Temporal dynamics of the magnetic fluxes, which are calculated for the magnetic field absolute value (black), vertical (orange) and horizontal (red) components. (c) Time profiles of the average magnetic field values in the flare ribbons. Colors mark different magnetic field components, similar to (b). The cyan and blue lines mark the GOES 1-8 Å lightcurve and its time derivative, respectively.

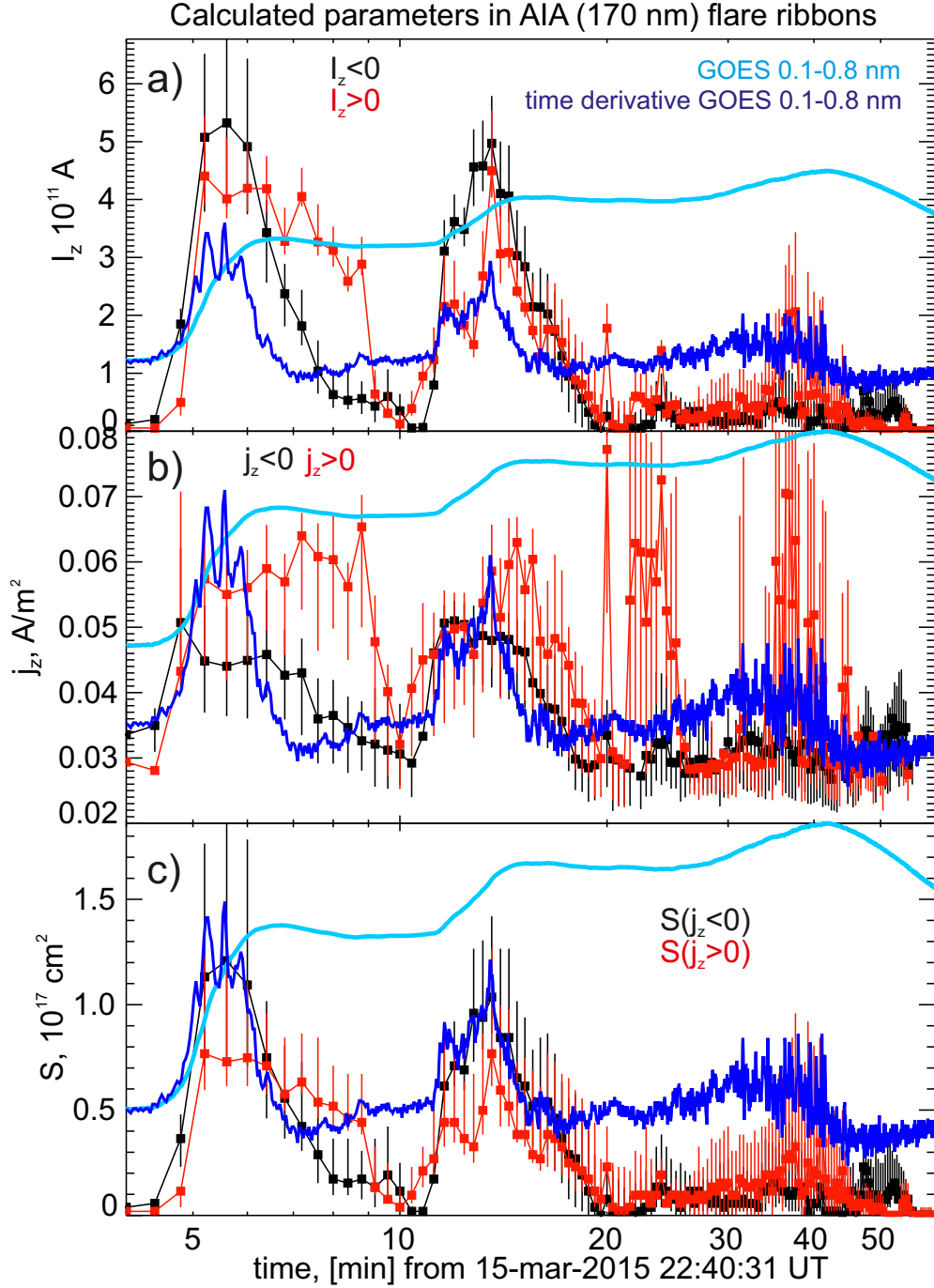


Fig. 15.— (a) Time profiles of the total PVEC inside the flare ribbons. (b) Time profiles of the averaged PVEC density inside the flare ribbons. (c) Time profiles of the total area characterizing the regions with strong PVEC within the flare ribbons. Estimates of the measurement errors are shown by the vertical bars. The red and black colors correspond to positive and negative electric currents, respectively. The cyan and blue lines mark the GOES 1-8 Å lightcurve and its time derivative, respectively. Note that time is on a logarithmic scale on the horizontal axis.

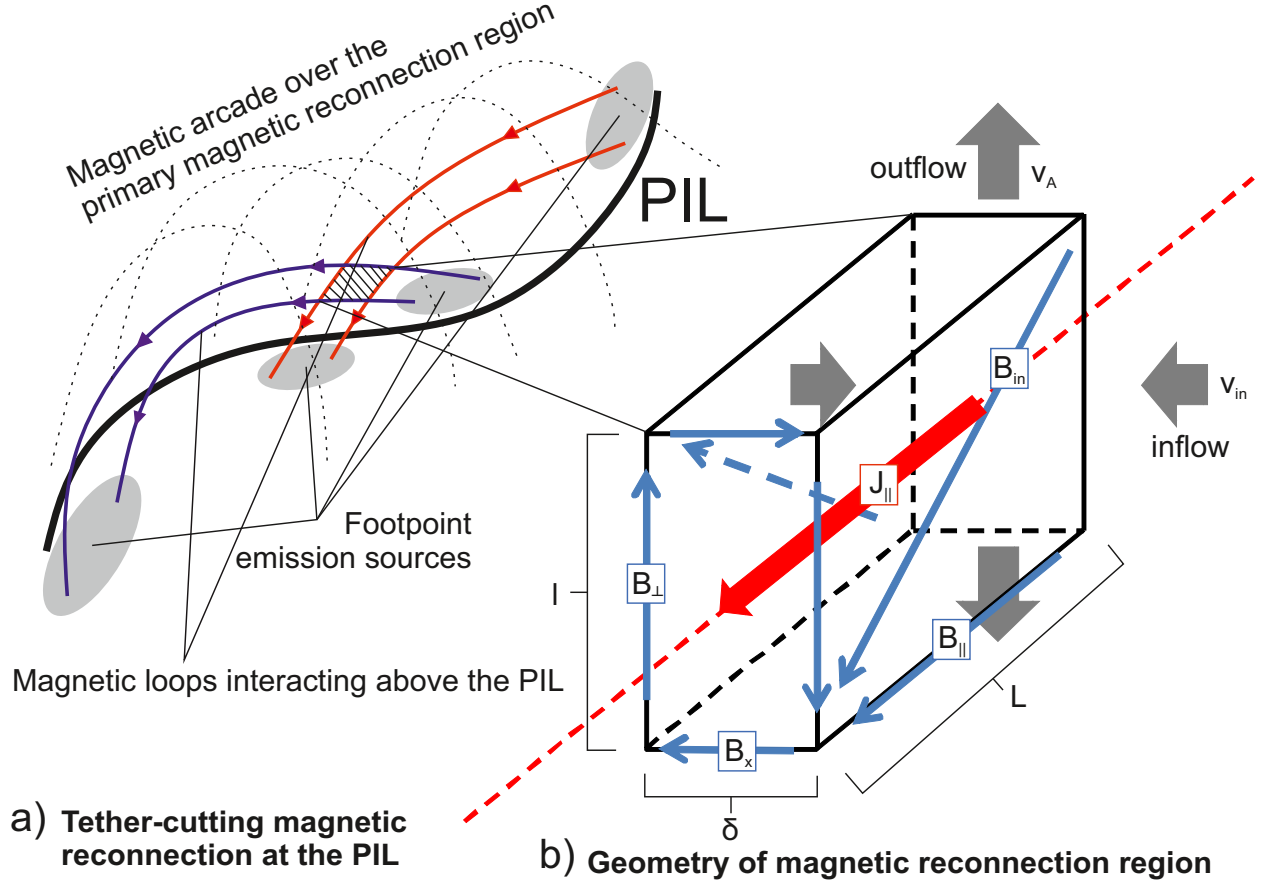


Fig. 16.— This scheme presents geometry of the magnetic reconnection region. Panel (a) describes general magnetic field topology in the frame of the TCMR scenario. Panel (b) shows magnetic field structure and geometry of the magnetic reconnection region.

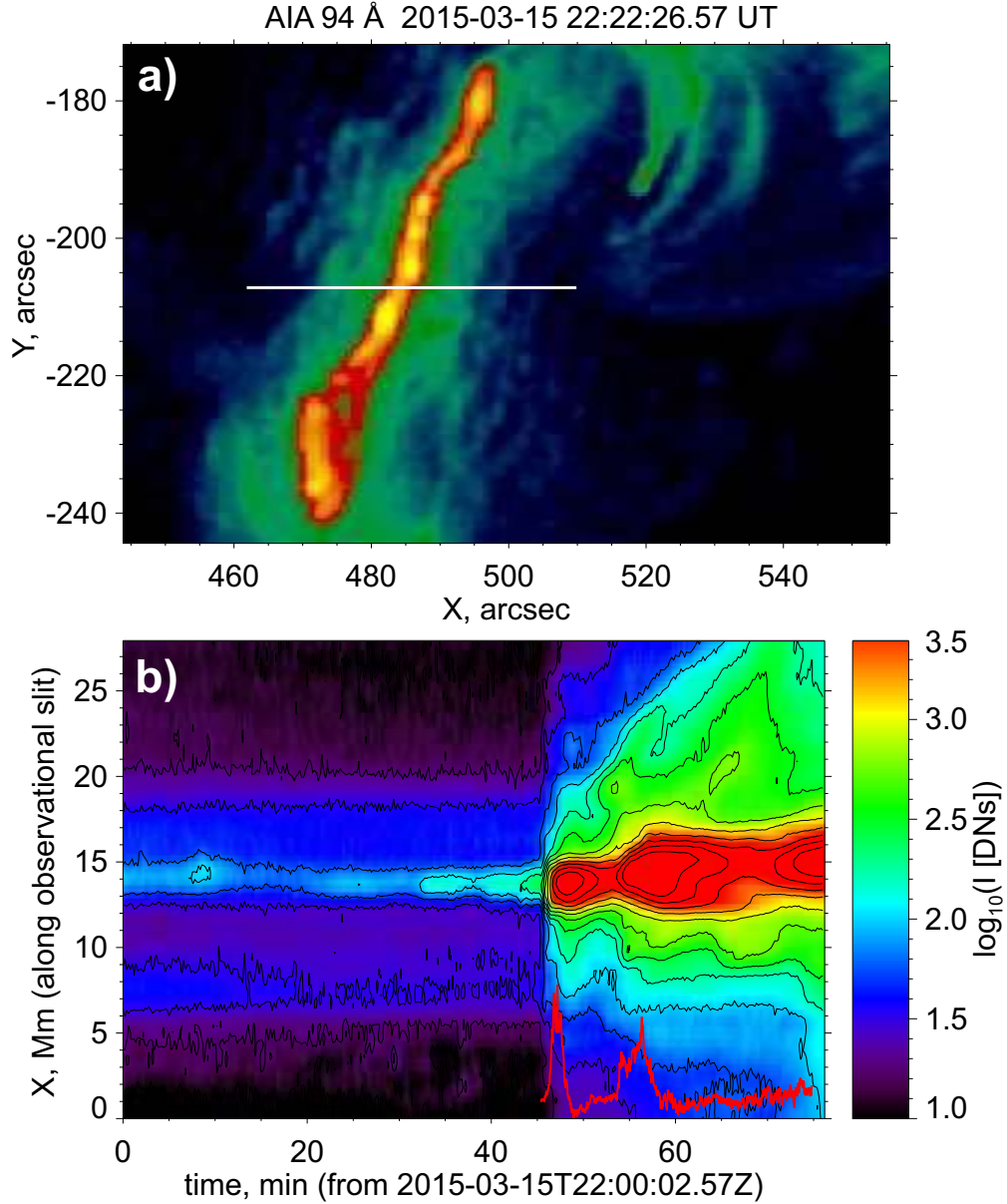


Fig. 17.— (a) The UV AIA 94 Å image of the active region made around 20 min before the flare impulsive phase onset, showing the presence of the bright worm-shaped structure above the PIL. The white horizontal line marks the slit used to make the time-distance plot, shown on (b), to trace the dynamics of the flare energy release around the PIL. To show the time-distance plot with more contrast we overplotted it with the black contours. Both color plots on (a) and (b) are made on a logarithmic scale of intensities. Red curve in the right-bottom part of panel (b) marks the time derivative of GOES 1-8 Å lightcurve to show the flare energy release rate. Note that time is on a linear scale on the horizontal axis.

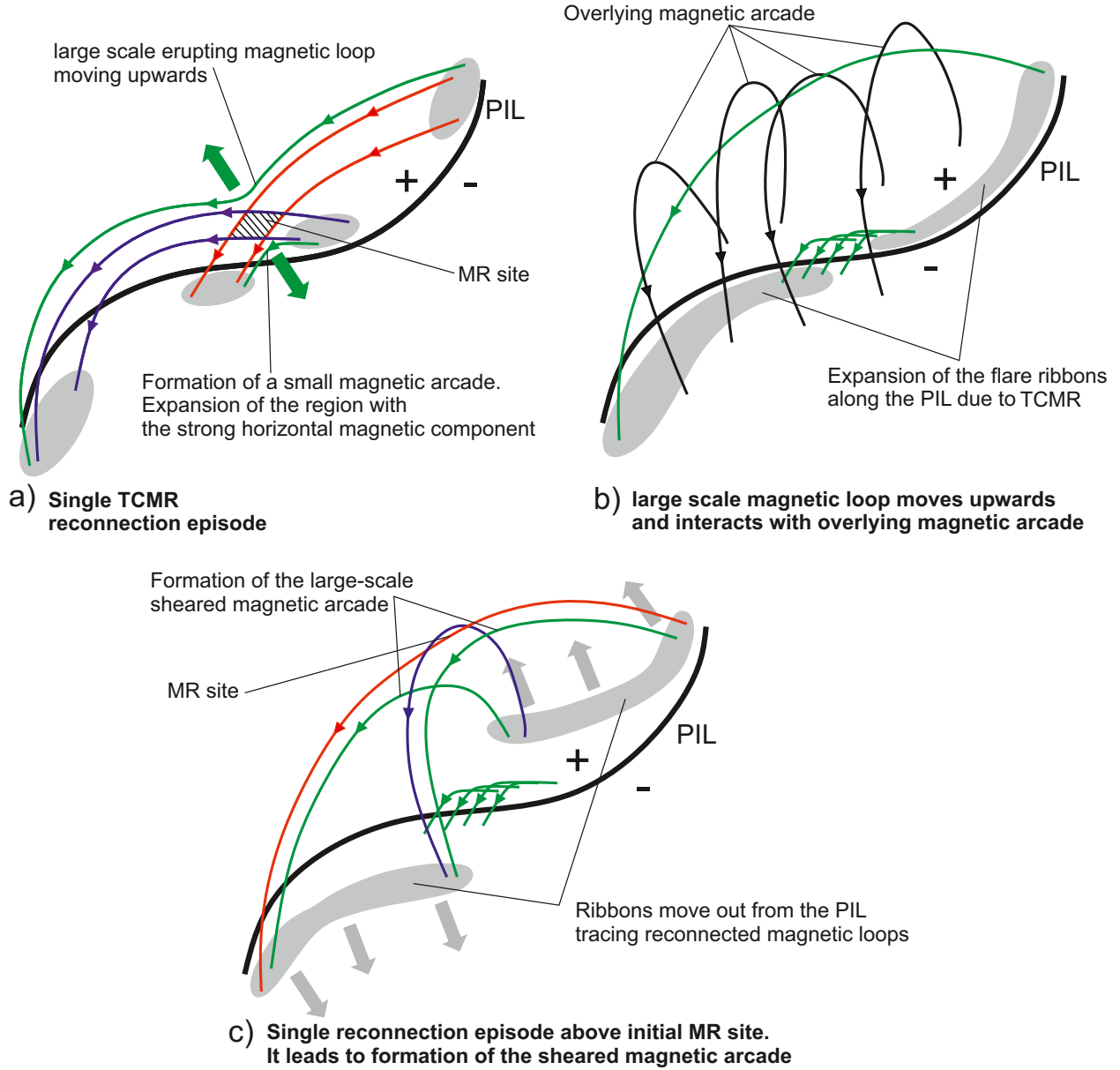


Fig. 18.— This scheme shows our explanations of the flare energy release process. Panel (a) demonstrates the flare onset as TCMR. Then upward moving magnetic field lines interact with the overlying magnetic arcade (panel (b)) that leads to the secondary magnetic reconnection (panel (c)) and cause flare ribbons to move from the PIL.